6 A Tutorial on Density Functional Theory

Fernando Nogueira*, Alberto Castro†,
and Miguel A.L. Marques‡

* Departamento de Física,
Universidade de Coimbra,
Rua Larga, 3004 – 516, Coimbra, Portugal
fnog@teor.fis.uc.pt

† Departamento de Física Teórica,
Universidad de Valladolid,
E–47011 Valladolid, Spain
alberto.castro@tddft.org

‡ Donostia International Physics Center (DIPC),
P. Manuel Lardizábal 4,
20080 San Sebastián, Spain
marques@tddft.org

Fernando Nogueira

6.1 Introduction

The success of density functional theory (DFT) is clearly demonstrated by the overwhelming amount of research articles describing results obtained within DFT that were published in the last decades. There is also a fair number of books reviewing the basics of the theory and its extensions (e.g., the present volume, [1] and [2]). These works fall mainly into three classes: those dealing with the theory (proposing extensions, new functionals, etc.), those concerned with the technical aspects of the numerical implementations, and others – the vast majority – presenting results. In our opinion, any scientist working in the field should have a sound knowledge of the three classes. For example, a theorist developing a new functional should be aware of the difficulties in implementing it. Or the applied scientist, performing calculations on specific systems, should know the limitations of the theory and of the numerical implementation she/he is using. The goal of this chapter is to supply the beginner with a brief pedagogical overview of DFT, combining the above-mentioned aspects. However, we will not review its foundations – we redirect the reader to the chapter of J. Perdew and S. Kurth that opens this book. Obviously, we will not be able to provide many details, but we hope that the beginner obtains a general impression of the capabilities and limitations of DFT.

This chapter is written in the form of a tutorial, combining basic theoretical and numerical aspects with specific examples, running from the simplest hydrogen atom to more complex molecules and solids. For the examples we used only freely available codes [3], so that the reader may easily reproduce

C. Fiolhais, F. Nogueira, M. Marques (Eds.): LNP 620, pp. 218–256, 2003.

the calculations. All input and output files can be found in the web site `http://www.tddft.org/DFT2001/`. The chapter follows closely the outline of the practical sessions held at Caramulo, during the DFT2001 summer school. Some theoretical or numerical aspects that were required in the practical sessions were, however, not covered by any of the lectures in Caramulo (e.g., pseudo-potentials). To fill this gap we provide in this chapter a brief account of some of them. We do not intend to discuss every possible numeric implementation of DFT. In particular, we do not include any explicit example of a localized basis set DFT calculation. Neither do we intend to present an extensive survey of the numerical aspects of each technique. We expect, however, that the technical details given are sufficient to enable the reader to perform himself the simulations presented herein.

The outline of the chapter is the following: We start, in Sect. 6.2, by giving a technical overview on how to solve the Kohn-Sham equations. The next section is devoted to pseudo-potentials, an essential ingredient of many DFT calculations. In Sect. 6.4 we present our first test case, namely atoms, before we proceed to some plane-wave calculations in Sect. 6.5. The final example, methane calculated using a real-space implementation, is presented in Sect. 6.6. We will use atomic units throughout this chapter, except when explicitly stated otherwise.

6.2 Solving the Kohn–Sham Equations

6.2.1 Generalities

It is usually stated that the Kohn-Sham equations are "simple" to solve. By "simple" it is meant that for a given system, e.g., an atom, a molecule, or a solid, the computational effort to solve the Kohn-Sham equations is smaller than the one required by the traditional quantum chemistry methods, like Hartree-Fock (HF) or configuration interaction (CI)[1]. But it does not mean that it is easy or quick to write, or even to use, a DFT based computer program. Typically, such codes have several thousand lines (for example, the ABINIT [4] package – a plane-wave DFT code – recently reached 200,000 lines) and hundreds of input options. Even writing a suitable input file is often a matter of patience and experience.

In spite of their differences, all codes try to solve the Kohn-Sham equations

$$\left[-\frac{\nabla^2}{2} + v_{\mathrm{KS}}[n](\boldsymbol{r})\right] \varphi_i(\boldsymbol{r}) = \varepsilon_i \varphi_i(\boldsymbol{r}) \; . \tag{6.1}$$

[1] This statement has to be taken with care, for it certainly depends on the approximation for the exchange-correlation potential. For example, it holds when using the local-density approximation or any of the generalized gradient approximations. However, if we use the exact exchange functional, the calculations are at least as computationally demanding as in Hartree-Fock.

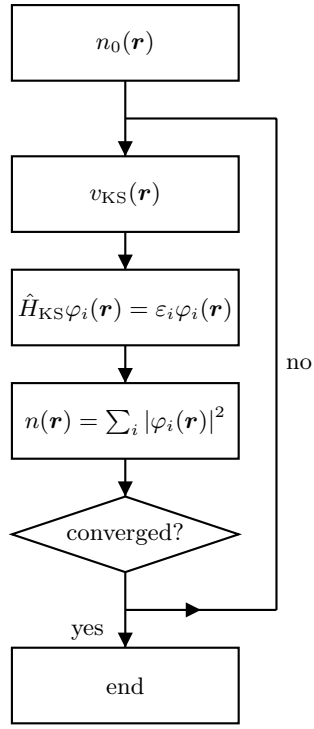

Fig. 6.1. Flow-chart depicting a generic Kohn-Sham calculation

The notation $v_{\rm KS}[n]$ means that the Kohn-Sham potential, $v_{\rm KS}$, has a functional dependence on n, the electronic density, which is defined in terms of the Kohn-Sham wave-functions by

$$n(\boldsymbol{r}) = \sum_{i}^{\rm occ} |\varphi_i(\boldsymbol{r})|^2 \, . \tag{6.2}$$

The potential $v_{\rm xc}$ is defined as the sum of the external potential (normally the potential generated by the nuclei), the Hartree term and the exchange and correlation (xc) potential

$$v_{\rm KS}[n](\boldsymbol{r}) = v_{\rm ext}(\boldsymbol{r}) + v_{\rm Hartree}[n](\boldsymbol{r}) + v_{\rm xc}[n](\boldsymbol{r}) \, . \tag{6.3}$$

Due to the functional dependence on the density, these equations form a set of nonlinear coupled equations. The standard procedure to solve it is iterating until self-consistency is achieved. A schematic flow chart of the scheme is depicted in Fig. 6.1. Usually one supplies some model density, $n_0(\boldsymbol{r})$, to start the iterative procedure. In principle, any positive function normalized to the total number of electrons would work, but using an educated guess for $n_0(\boldsymbol{r})$ can speed-up convergence dramatically. For example, in a molecular or a

solid-state system one could construct $n_0(\boldsymbol{r})$ from a sum of atomic densities

$$n_0(\boldsymbol{r}) = \sum_\alpha n_\alpha(\boldsymbol{r} - \boldsymbol{R}_\alpha) \,, \tag{6.4}$$

where $\boldsymbol{R}_\alpha$ and n_α represent the position and atomic density of the nucleus α. For an atom, a convenient choice is the Thomas-Fermi density.

We then evaluate the Kohn-Sham potential (see 6.3) with this density. Each of the components of $v_{\rm KS}$ is calculated separately and each of them poses a different numerical problem. The external potential is typically a sum of nuclear potentials centered at the atomic positions,

$$v_{\rm ext}(\boldsymbol{r}) = \sum_\alpha v_\alpha(\boldsymbol{r} - \boldsymbol{R}_\alpha) \,. \tag{6.5}$$

In some applications, v_α is simply the Coulomb attraction between the bare nucleus and the electrons, $v_\alpha(\boldsymbol{r}) = -Z_\alpha/r$, where Z_α is the nuclear charge. In other cases the use of the Coulomb potential renders the calculation unfeasible, and one has to resort to pseudo-potentials (see Sect. 6.3.1).

The next term in $v_{\rm KS}$ is the Hartree potential,

$$v_{\rm Hartree}(\boldsymbol{r}) = \int \mathrm{d}^3 r' \, \frac{n(\boldsymbol{r}')}{|\boldsymbol{r} - \boldsymbol{r}'|} \,. \tag{6.6}$$

There are several different techniques to evaluate this integral, either by direct integration (as it is done when solving the atomic Kohn-Sham equations), or by solving the equivalent differential (Poisson's) equation,

$$\nabla^2 v_{\rm Hartree}(\boldsymbol{r}) = -4\pi n(\boldsymbol{r}) \,. \tag{6.7}$$

As the choice of the best technique depends on the specific problem, we defer further discussion on the Hartree term to Sects. 6.2.2–6.2.4.

Finally, we have the xc potential, which is formally defined through the functional derivative of the xc energy,

$$v_{\rm xc}(\boldsymbol{r}) = \frac{\delta E_{\rm xc}}{\delta n(\boldsymbol{r})} \,. \tag{6.8}$$

Perhaps more than a hundred approximate xc functionals have appeared in the literature over the past 30 years. The first to be proposed and, in fact, the simplest of all, is the local-density approximation (LDA). It is written as

$$E_{\rm xc}^{\rm LDA} = \int \mathrm{d}^3 r \; \varepsilon^{\rm HEG}(n)\big|_{n=n(\boldsymbol{r})} \quad ; \quad v_{\rm xc}^{\rm LDA}(\boldsymbol{r}) = \frac{\mathrm{d}}{\mathrm{d}n} \, \varepsilon^{\rm HEG}(n)\big|_{n=n(\boldsymbol{r})} \,, \tag{6.9}$$

where $\varepsilon^{\rm HEG}(n)$ stands for the xc energy per unit volume of the homogeneous electron gas (HEG) of (constant) density n. Note that $\varepsilon^{\rm HEG}(n)$ is a simple *function* of n, which was tabulated for several densities using Monte Carlo

methods by Ceperley and Alder [5]. A number of different parameterizations exist for this function, like the PZ81 [6] and PW92 [7]. It is clear from these considerations that evaluating the LDA xc potential is as simple (and fast) as evaluating any rational or transcendental function. In the case of the generalized gradient approximations (GGA) the functional has a similar form, but now ε does not depend solely on the density n, but also on its gradient ∇n. The evaluation of the GGA xc potential is also fairly straightforward. Finally, we mention the third generation of density functionals, the orbital-dependent functionals (see the chapter by E. Engel in this book) like the exact exchange (EXX). In order to obtain the xc potential in this case, one is required to solve an integral equation[2]. This equation is quite complex, and its solution can easily become the most time-consuming part of the Kohn-Sham calculation. We should also notice that functionals like the EXX involve the evaluation of the so-called Coulomb integrals. These two-center integrals, that also appear in Hartree-Fock theory, pose another difficult problem to the computational physicist or chemist.

Now that we have the Kohn-Sham potential, we can solve the Kohn-Sham equation (6.1). The goal is to obtain the p lowest eigenstates of the Hamiltonian H_{KS}, where p is half the number of electrons (for a spin-unpolarized calculation). For an atom, or for any other case where the Kohn-Sham equations can be reduced to a one-dimensional differential equation, a very efficient integration method is commonly employed (see below). In other cases, when using basis sets, plane-waves, or real-space methods, one has to diagonalize the Hamiltonian matrix, $\hat{H}_{\mathrm{KS}}$. We have to keep in mind that fully diagonalizing a matrix is a q^3 problem, where q is the dimension of the matrix (which is roughly proportional to the number of atoms in the calculation). Moreover, the dimension of the Hamiltonian is sometimes of the order of $10^6 \times 10^6 = 10^{12}$ elements[3]. It is clearly impossible to store such a matrix in any modern computer. To circumvent these problems, one usually resorts to iterative methods. In these methods it is never necessary to write the full Hamiltonian – the knowledge of how $\hat{H}_{\mathrm{KS}}$ applies to a test wave-function is sufficient. These methods also scale much better with the dimension of the matrix. Nonetheless, diagonalizing the Kohn-Sham Hamiltonian is usually the most time-consuming part of an ordinary Kohn-Sham calculation.

We have now all the ingredients to obtain the electronic density from (6.2). The self-consistency cycle is stopped when some convergence criterion is reached. The two most common criteria are based on the difference of total energies or densities from iteration i and $i-1$, i.e., the cycle is stopped when $\left|E^{(i)} - E^{(i-1)}\right| < \eta_E$ or $\int \mathrm{d}^3 r \left|n^{(i)} - n^{(i-1)}\right| < \eta_n$, where $E^{(i)}$ and $n^{(i)}$ are the total energy and density at iteration i, and η_E and η_n are user defined tolerances. If, on the contrary, the criteria have not been fulfilled, one restarts

[2] Or choose to apply the Krieger, Lee and Iafrate approximation [8].

[3] However, $\hat{H}_{\mathrm{KS}}$ is usually a very sparse matrix. For example, in a typical real-space calculation only less than.1 % of the elements of $\hat{H}$ are different from 0.

the self-consistency cycle with a new density. It could simply be the output density of the previous cycle – unfortunately this would almost certainly lead to instabilities. To avoid them, one usually mixes this output density with densities from previous iterations. In the simplest scheme, linear mixing, the density supplied to start the new iteration, $n^{(i+1)}$ is a linear combination of the density obtained from (6.2), n', and the density of the previous iteration, $n^{(i)}$,

$$n^{(i+1)} = \beta n' + (1-\beta) n^{(i)} \,, \tag{6.10}$$

where the parameter β is typically chosen to be around 0.3. More sophisticated mixing schemes have been proposed (e.g., Anderson or Broyden mixing [9,10,11,12,13]), in which $n^{(i+1)}$ is an educated extrapolation of the densities of several previous iterations.

At the end of the calculation, we can evaluate several observables, the most important of which is undoubtedly the total energy. From this quantity, one can obtain, e.g., equilibrium geometries, phonon dispersion curves, or ionization potentials. In Kohn-Sham theory, the total energy is written as

$$\begin{aligned} E = &- \sum_i^{\text{occ}} \int \mathrm{d}^3 r \, \varphi_i^*(\boldsymbol{r}) \frac{\nabla^2}{2} \varphi_i(\boldsymbol{r}) + \int \mathrm{d}^3 r \, v_{\text{ext}}(\boldsymbol{r}) n(\boldsymbol{r}) + \\ &+ \frac{1}{2} \int \mathrm{d}^3 r \int \mathrm{d}^3 r' \, \frac{n(\boldsymbol{r}) n(\boldsymbol{r}')}{|\boldsymbol{r} - \boldsymbol{r}'|} + E_{\text{xc}} \,, \end{aligned} \tag{6.11}$$

where the terms are respectively the non-interacting (Kohn-Sham) kinetic energy, the external potential, the Hartree and the xc energies. This formula can be further simplified by using the Kohn-Sham equation, (see 6.1), to yield

$$E = \sum_i^{\text{occ}} \varepsilon_i - \int \mathrm{d}^3 r \, \left[\frac{1}{2} v_{\text{Hartree}}(\boldsymbol{r}) + v_{\text{xc}}(\boldsymbol{r}) \right] n(\boldsymbol{r}) + E_{\text{xc}} \,. \tag{6.12}$$

This is the formula implemented in most DFT codes. Note that, when performing geometry optimization or nuclear dynamics, one needs to add to the total energy a repulsive Coulomb term that accounts for the interactions between the ions

$$E_{\text{nn}} = \sum_{\alpha,\beta} \frac{Z_\alpha Z_\beta}{|\boldsymbol{R}_\alpha - \boldsymbol{R}_\beta|} \,. \tag{6.13}$$

Calculating the sum over all atoms is fairly straightforward for finite systems, but non-trivial for extended systems: As the Coulomb interaction is very long ranged, the (infinite) sum in (6.13) is very slowly convergent. There is, however, a technique due to Ewald that allows us to circumvent this problem and evaluate (6.13) (see Sect. 6.2.3).

6.2.2 Atoms

In order to solve the Kohn-Sham equations (6.1) for atoms, one normally performs a spherical averaging of the density[4]. This averaging leads to a spherically symmetric Kohn-Sham potential. The Hartree potential is then trivially evaluated as

$$v_{\mathrm{Hartree}}(r) = \frac{4\pi}{r}\int_0^r \mathrm{d}r'\; r'^2 n(r') + 4\pi\int_r^\infty \mathrm{d}r'\; r' n(r') \; . \tag{6.14}$$

and the Kohn-Sham wave-functions can be written as the product of a radial wave-function, $R_{nl}(r)$, and a spherical harmonic, $Y_{lm}(\theta,\phi)$:

$$\varphi_i(\boldsymbol{r}) = R_{nl}(r) Y_{lm}(\theta,\phi) \; . \tag{6.15}$$

The wave-functions are labeled using the traditional atomic quantum numbers: n for the principal quantum number and l, m for the angular momentum. The Kohn-Sham equation then becomes a "simple" one-dimensional second-order differential equation

$$\left[-\frac{1}{2}\frac{\mathrm{d}^2}{\mathrm{d}r^2} - \frac{1}{r}\frac{\mathrm{d}}{\mathrm{d}r} + \frac{l(l+1)}{2r^2} + v_{\mathrm{KS}}(r)\right] R_{nl}(r) = \varepsilon_{nl} R_{nl}(r) \; , \tag{6.16}$$

that can be transformed into two coupled first-order differential equations

$$\begin{aligned} &\frac{\mathrm{d}f_{nl}(r)}{\mathrm{d}r} = g_{nl}(r) \\ &\frac{\mathrm{d}g_{nl}(r)}{\mathrm{d}r} + \frac{2}{r} g_{nl}(r) - \frac{l(l+1)}{r^2} f_{nl}(r) + 2\left\{\varepsilon_{nl} - v_{\mathrm{KS}}(r)\right\} f_{nl}(r) = 0 \; , \end{aligned} \tag{6.17}$$

where $f_{nl}(r) \equiv R_{nl}(r)$.

When $r \to \infty$, the coupled equations become

$$\begin{aligned} &\frac{\mathrm{d}f_{nl}(r)}{\mathrm{d}r} = g_{nl}(r) \\ &\frac{\mathrm{d}g_{nl}(r)}{\mathrm{d}r} + 2\varepsilon_{nl} f_{nl}(r) \simeq 0 \; , \end{aligned} \tag{6.18}$$

provided that the Kohn-Sham potential goes to zero at large distances from the atom (which it does, see Fig. 6.6). This indicates that the solutions of (6.17) should behave asymptotically as

$$\begin{aligned} f_{nl}(r) &\overset{r\to\infty}{\longrightarrow} \mathrm{e}^{-\sqrt{-2\varepsilon_{nl}}r} \\ g_{nl}(r) &\overset{r\to\infty}{\longrightarrow} -\sqrt{-2\varepsilon_{nl}} f_{nl}(r) \; . \end{aligned} \tag{6.19}$$

[4] Although the assumption of a spherically symmetric potential (density) is only strictly valid in a closed shell system, the true many-body potential is indeed spherically symmetric. For open shell systems this assumption implies an identical filling of all degenerate atomic orbitals.

At the origin ($r \to 0$) the solutions are of the form

$$f_{nl}(r) \stackrel{r\to 0}{\longrightarrow} Ar^{\alpha} \qquad (6.20)$$
$$g_{nl}(r) \stackrel{r\to 0}{\longrightarrow} Br^{\beta} \ .$$

Substituting (6.20) into (6.17) gives $B = lA$, $\alpha = l$, and $\beta = l - 1$.

For a fixed ε_{nl} and A it is a simple task to integrate (6.17) from $r = 0$ to ∞ using (6.20) to provide the initial values. However, if ε_{nl} is not an eigenvalue of (6.16), the solution will diverge (i.e., it will not obey boundary conditions at infinity (6.19)). Fortunately, there is a simple procedure to obtain the ε_{nl} that yield solutions with the correct asymptotic behavior. The technique involves integrating (6.20) from $r = 0$ to a conveniently chosen point r_m (e.g., the classical turning point), and at the same time integrating (6.20) starting from a point very far away ("practical infinity", r_∞) to r_m. From the two values of $f_{nl}(r_m)$ and $g_{nl}(r_m)$ obtained in this way, it is then possible to improve our estimate of ε_{nl}.

The technique for simultaneously finding the eigenvalues ε_{nl} and the wave-functions proceeds as follows:

i) Choose an arbitrary value for ε_{nl} and $f_{nl}(r_\infty)$;
ii) Calculate $g_{nl}(r_\infty)$ using the boundary conditions (6.19);
iii) Integrate (6.17) from r_∞ to r_m (to get $f_{nl}^{\text{in}}(r)$ and $g_{nl}^{\text{in}}(r)$);
iv) Choose an arbitrary value for A, calculate $B = lA$, and use the boundary conditions (6.20) to get $f_{nl}(0)$ and $g_{nl}(0)$;
v) Integrate (6.17) from 0 to r_m (to get $f_{nl}^{\text{out}}(r)$ and $g_{nl}^{\text{out}}(r)$);
vi) Calculate $\gamma = g_{nl}^{\text{in}}(r_m)/g_{nl}^{\text{out}}(r_m)$ and scale $f_{nl}^{\text{out}}(r)$ and $g_{nl}^{\text{out}}(r)$ by this factor – now $g_{nl}(r)$ is continuous at the matching point ($\tilde{g}_{nl}^{\text{out}}(r_m) \equiv \gamma g_{nl}^{\text{out}}(r_m) = g_{nl}^{\text{in}}(r_m)$) but $f_{nl}(r)$ is not;
vii) Compute $\delta(\varepsilon_{nl}) = f_{nl}^{\text{out}}(r_m) - f_{nl}^{\text{in}}(r_m)$: The zeros of this function are the eigenvalues, so one can find them using, e.g., the bisection method (one has to provide an educated guess for the minimum and maximum value of the eigenvalues).

6.2.3 Plane-Waves

To calculate the total energy of solids, a plane-wave expansion of the Kohn-Sham wave-functions is very useful, as it takes advantage of the periodicity of the crystal [14,15,16]. For finite systems, such as atoms, molecules and clusters, plane-waves can also be used in a super-cell approach[5]. In this method,

[5] The super-cell technique is restricted in its usual form to neutral systems due to the long-range interaction between a charged cluster and its periodic images: the Coulomb energy for charged periodic systems diverges and must be removed. Some common methods used to circumvent this difficulty are: i) To introduce a compensating jellium background that neutralizes the super-cell [17]; ii) To use a cutoff in the Coulomb interaction [18]; iii) To shield each charged cluster with a spherical shell having a symmetric charge which neutralizes the super-cell and cancels the electric dipole of the charged cluster [19].

the finite system is placed in a unit cell of a fictitious crystal, and this cell is made large enough to avoid interactions between neighboring cells. The Kohn-Sham equations can then be solved, for any system, in momentum space. However, for finite systems a very large number of plane-waves is needed as the electronic density is concentrated on a small fraction of the total volume of the super-cell.

The valence wave-functions of the large Z atoms oscillate strongly in the vicinity of the atomic core due to the orthogonalization to the inner electronic wave-functions. To describe these oscillations a large number of plane-waves is required, difficulting the calculation of the total energy. However, the inner electrons are almost inert and are not significantly involved in bonding. This suggests the description of an atom based solely on its valence electrons, which feel an effective potential including both the nuclear attraction and the repulsion of the inner electrons. This approximation, the pseudo-potential approximation, will be presented in more detail in Sect. 6.3.1.

When using the pseudo-potential approximation, the external potential, v_{ext}, is simply the sum of the pseudo-potentials of all the atoms in the system. If atom α is located in the unit cell at $\boldsymbol{\tau}_\alpha$ and its pseudo-potential is $w_\alpha(\boldsymbol{r}, \boldsymbol{r}')$, the external potential is

$$w(\boldsymbol{r}, \boldsymbol{r}') = \sum_{j,\alpha} w_\alpha(\boldsymbol{r} - \boldsymbol{R}_j - \boldsymbol{\tau}_\alpha, \boldsymbol{r}' - \boldsymbol{R}_j - \boldsymbol{\tau}_\alpha) \;, \tag{6.21}$$

where $\boldsymbol{R}_j$ are the lattice vectors. The pseudo-potential is considered in its more general non-local form, which implies that the second term of the right-hand side of (6.11) is rewritten as

$$\int \mathrm{d}^3 r \, v_{\text{ext}}(\boldsymbol{r}) n(\boldsymbol{r}) \longrightarrow \sum_{i=1}^{N} \int \mathrm{d}^3 r \int \mathrm{d}^3 r' \, \varphi_i(\boldsymbol{r}) w(\boldsymbol{r}, \boldsymbol{r}') \varphi_i^*(\boldsymbol{r}') \;. \tag{6.22}$$

According to Bloch's theorem, the Kohn-Sham wave-functions, $\varphi_{\boldsymbol{k},n}(\boldsymbol{r})$, can be written as

$$\varphi_{\boldsymbol{k},n}(\boldsymbol{r}) = \mathrm{e}^{\mathrm{i}\boldsymbol{k}\cdot\boldsymbol{r}} \sum_{\boldsymbol{G}} c_{\boldsymbol{k},n}(\boldsymbol{G}) \mathrm{e}^{\mathrm{i}\boldsymbol{G}\cdot\boldsymbol{r}} \;, \tag{6.23}$$

where $\boldsymbol{k}$ is the wave vector, n the band index, and $\boldsymbol{G}$ are the reciprocal lattice vectors. The Kohn-Sham energies are $\varepsilon_{\boldsymbol{k},n}$, and the electronic density is

$$n(\boldsymbol{r}) = \sum_{\boldsymbol{k},n} \sum_{\boldsymbol{G},\boldsymbol{G}'} f(\varepsilon_{\boldsymbol{k},n}) c^*_{\boldsymbol{k},n}(\boldsymbol{G}') c_{\boldsymbol{k},n}(\boldsymbol{G}) \mathrm{e}^{\mathrm{i}(\boldsymbol{G}-\boldsymbol{G}')\cdot\boldsymbol{r}} \;, \tag{6.24}$$

where the $f(\varepsilon_{\boldsymbol{k},n})$ denote the occupation numbers. The Fourier transform of the density is

$$n(\boldsymbol{G}) = \sum_{\boldsymbol{k},n} \sum_{\boldsymbol{G}'} f(\varepsilon_{\boldsymbol{k},n}) c^*_{\boldsymbol{k},n}(\boldsymbol{G}' - \boldsymbol{G}) c_{\boldsymbol{k},n}(\boldsymbol{G}') \;. \tag{6.25}$$

The sums over $\boldsymbol{k}$ are performed over all Brillouin zone vectors, but can be reduced to sums on the irreducible Brillouin zone by taking advantage of the space group of the lattice[6].

There are thus two convergence parameters that need to be fine-tuned for every calculation: the Brillouin zone sampling and a cutoff radius in reciprocal space to truncate the sums over reciprocal lattice vectors (we cannot perform infinite summations!)

The kinetic energy is rewritten as

$$T = \frac{1}{2} \sum_{\boldsymbol{k},n} \sum_{\boldsymbol{G}} f(\varepsilon_{\boldsymbol{k},n}) \left| c_{\boldsymbol{k},n}(\boldsymbol{G}) \right|^2 \left| \boldsymbol{k} + \boldsymbol{G} \right|^2 \ , \tag{6.26}$$

and the Hartree energy is given by

$$E_{\text{Hartree}} = \frac{\Omega}{2} \sum_{\boldsymbol{G}} v_{\text{Hartree}}(\boldsymbol{G}) n(\boldsymbol{G}) \ , \tag{6.27}$$

where Ω is the unit cell volume and the Hartree potential, $v_{\text{Hartree}}(\boldsymbol{G})$, is obtained using Poisson's equation

$$v_{\text{Hartree}}(\boldsymbol{G}) = 4\pi \frac{n(\boldsymbol{G})}{G^2} \ . \tag{6.28}$$

The electron-ion interaction energy, (6.22), is given by

$$E_{\text{ei}} = \sum_{\boldsymbol{k},n} \sum_{\boldsymbol{G},\boldsymbol{G}'} f(\varepsilon_{\boldsymbol{k},n}) c^*_{\boldsymbol{k},n}(\boldsymbol{G}) c_{\boldsymbol{k},n}(\boldsymbol{G}') w(\boldsymbol{k}+\boldsymbol{G}, \boldsymbol{k}+\boldsymbol{G}') \ , \tag{6.29}$$

and the Fourier transform of the total pseudo-potential is

$$w(\boldsymbol{k}+\boldsymbol{G}, \boldsymbol{k}+\boldsymbol{G}') = \sum_{\alpha} w_\alpha(\boldsymbol{k}+\boldsymbol{G}, \boldsymbol{k}+\boldsymbol{G}') \mathrm{e}^{\mathrm{i}(\boldsymbol{G}-\boldsymbol{G}')\cdot\boldsymbol{\tau}_\alpha} \ . \tag{6.30}$$

The Fourier transform of the individual pseudo-potentials, $v_\alpha(\boldsymbol{k}, \boldsymbol{k}')$, can be written in a simple form if the separable Kleinmnan and Bylander form is used (see Sect. 6.3.8).

Both E_{ei} (due to the local part of the pseudo-potential) and the Hartree potential diverge at $\boldsymbol{G} = 0$. The ion-ion interaction energy, E_{nn}, also diverges. However, the sum of these three divergent terms is a constant, if the system is electrically neutral. This constant is [14,15,16]

$$\lim_{\boldsymbol{G},\boldsymbol{G}'\to 0} \left[\sum_{\boldsymbol{k},n} f(\varepsilon_{\boldsymbol{k},n}) c^*_{\boldsymbol{k},n}(\boldsymbol{G}) c_{\boldsymbol{k},n}(\boldsymbol{G}') w(\boldsymbol{k}+\boldsymbol{G}, \boldsymbol{k}+\boldsymbol{G}') + \right.$$
$$\left. + \frac{\Omega}{2} v_{\text{Hartree}}(\boldsymbol{G}) n(\boldsymbol{G}) \right] + E_{\text{nn}} = E_{\text{rep}} + E_{\text{Ewald}} \ , \tag{6.31}$$

[6] To further simplify these sums, it is possible to do a smart sampling of the irreducible Brillouin zone, including in the sums only some special $\boldsymbol{k}$ vectors [20,21,22,23].

where

$$E_{\rm rep} = Z_{\rm total} \frac{1}{\Omega} \sum_{\alpha} \Lambda_{\alpha} \tag{6.32}$$

and

$$\Lambda_{\alpha} = \frac{1}{\Omega} \int {\rm d}^3 r \left[v_{\alpha,{\rm local}}(r) + \frac{Z_{\alpha}}{r} \right] . \tag{6.33}$$

In these expressions Z_{α} is the electric charge of ion α, and $v_{\alpha,{\rm local}}(r)$ is the local part of the pseudo-potential of atom α (equations (6.74) and (6.75)). The non-divergent part of the ion-ion interaction energy, $E_{\rm Ewald}$, is calculated using a trick due to Ewald [24]. One separates it in two parts, one short-ranged that is summed in real space, and a long-range part that is treated in Fourier space. By performing this splitting, one transforms a slowly convergent sum into two rapidly convergent sums

$$E_{\rm Ewald} = \frac{1}{2} \sum_{\alpha,\alpha'} Z_{\alpha} \Gamma_{\alpha,\alpha'} Z_{\alpha'} , \tag{6.34}$$

with the definition

$$\begin{aligned} \Gamma_{\alpha,\alpha'} = \frac{4\pi}{\Omega} \sum_{\boldsymbol{G} \neq 0} \frac{\cos\left[\boldsymbol{G} \cdot (\boldsymbol{\tau}_{\alpha} - \boldsymbol{\tau}_{\alpha'})\right]}{G^2} {\rm e}^{-\frac{G^2}{4\eta^2}} + \\ + \sum_{j} \frac{{\rm erfc}\left(\eta \left| \boldsymbol{R}_j + \boldsymbol{\tau}_{\alpha} - \boldsymbol{\tau}_{\alpha'} \right|\right)}{\left| \boldsymbol{R}_j + \boldsymbol{\tau}_{\alpha} - \boldsymbol{\tau}_{\alpha'} \right|} - \frac{\pi}{\eta^2 \Omega} - \frac{2\eta}{\sqrt{\pi}} \delta_{\alpha\alpha'} . \end{aligned} \tag{6.35}$$

(erfc(x) is the complimentary error function.) Note that this term has only to be evaluated once at the beginning of the self-consistency cycle, for it does not depend on the density. The parameter η is arbitrary, and is chosen such that the two sums converge quickly.

In momentum space, the total energy is then

$$E_{\rm tot} = T + E'_{\rm Hartree} + E'_{\rm ei} + E_{\rm xc} + E_{\rm Ewald} + E_{\rm rep} , \tag{6.36}$$

with the terms $\boldsymbol{G}, \boldsymbol{G}' = 0$ excluded from the Hartree and pseudo-potential contributions. Finally, the Kohn-Sham equations become

$$\sum_{\boldsymbol{G}'} \hat{H}_{\boldsymbol{G},\boldsymbol{G}'}(\boldsymbol{k}) c_{\boldsymbol{k},n}(\boldsymbol{G}') = \varepsilon_{\boldsymbol{k},n} c_{\boldsymbol{k},n}(\boldsymbol{G}) , \tag{6.37}$$

where

$$\begin{aligned} \hat{H}_{\boldsymbol{G},\boldsymbol{G}'}(\boldsymbol{k}) = \frac{1}{2} \left| \boldsymbol{k} + \boldsymbol{G} \right|^2 \delta_{\boldsymbol{G},\boldsymbol{G}'} + \\ + w(\boldsymbol{k} + \boldsymbol{G}, \boldsymbol{k} + \boldsymbol{G}') + v_{\rm Hartree}(\boldsymbol{G} - \boldsymbol{G}') + v_{\rm xc}(\boldsymbol{G} - \boldsymbol{G}') , \end{aligned} \tag{6.38}$$

and are solved by diagonalizing the Hamiltonian.

6.2.4 Real-Space

In this scheme, functions are not expanded in a basis set, but sampled in a real-space mesh [25]. This mesh is commonly chosen to be uniform (the points are equally spaced in a cubic lattice), although other options are possible. Convergence of the results has obviously to be checked against the grid spacing. One big advantage of this approach is that the potential operator is diagonal. The Laplacian operator entering the kinetic energy is discretized at the grid points $\boldsymbol{r}_i$ using a finite order rule,

$$\nabla^2 \varphi(\boldsymbol{r}_i) = \sum_j c_j \varphi(\boldsymbol{r}_j) \; . \tag{6.39}$$

For example, the lowest order rule in one dimension, the three point rule reads

$$\left.\frac{\mathrm{d}^2}{\mathrm{d}r^2}\varphi(r)\right|_{r_i} = \frac{1}{4}\left[\varphi(r_{i-1}) - 2\varphi(r_i) + \varphi(r_{i+1})\right] \; . \tag{6.40}$$

Normally, one uses a 7 or 9-point rule.

Another important detail is the evaluation of the Hartree potential. It cannot be efficiently obtained by direct integration of (6.6). There are however several other options: (i) solving Poisson's equation, (6.7), in Fourier space – as in the plane-wave method; (ii) recasting (6.7) into a minimization problem and applying, e.g., a conjugate gradients technique; (iii) using multi-grid methods [25,26,27]. The last of the three is considered to be the most efficient technique.

In our opinion, the main advantage of real-space methods is the simplicity and intuitiveness of the whole procedure. First of all, quantities like the density or the wave-functions are very simple to visualize in real space. Furthermore, the method is fairly simple to implement numerically for 1-, 2-, or 3-dimensional systems, and for a variety of different boundary conditions. For example, one can study a finite system, a molecule, or a cluster without the need of a super-cell, simply by imposing that the wave-functions are zero at a surface far enough from the system. In the same way, an infinite system, a polymer, a surface, or bulk material can be studied by imposing the appropriate cyclic boundary conditions. Note also that in the real-space method there is only one convergence parameter, namely the grid-spacing.

Unfortunately, real-space methods suffer from a few drawbacks. For example, most of the real-space implementations are not variational, i.e., we may find a total energy lower than the true energy, and if we reduce the grid-spacing the energy can actually increase. Moreover, the grid breaks translational symmetry, and can also break other symmetries that the system may possess. This can lead to the artificial lifting of some degeneracies, to the appearance of spurious peaks in spectra, etc. Of course all these problems can be minimized by reducing the grid-spacing.

6.3 Pseudo-potentials

6.3.1 The Pseudo-potential Concept

The many-electron Schrödinger equation can be very much simplified if electrons are divided in two groups: valence electrons and inner core electrons. The electrons in the inner shells are strongly bound and do not play a significant role in the chemical binding of atoms, thus forming with the nucleus an (almost) inert core. Binding properties are almost completely due to the valence electrons, especially in metals and semiconductors.

This separation suggests that inner electrons can be ignored in a large number of cases, thereby reducing the atom to a ionic core that interacts with the valence electrons. The use of an effective interaction, a pseudo-potential, that approximates the potential felt by the valence electrons, was first proposed by Fermi in 1934 [28]. Hellmann in 1935 [29] suggested that the form

$$w(r) = -\frac{1}{r} + \frac{2.74}{r}\mathrm{e}^{-1.16r} \tag{6.41}$$

could represent the potential felt by the valence electron of potassium. In spite of the simplification pseudo-potentials introduce in calculations, they remained forgotten until the late 50's. It was only in 1959, with Phillips and Kleinman [30,31,32], that pseudo-potentials began to be extensively used.

Let the exact solutions of the Schrödinger equation for the inner electrons be denoted by $|\psi_c\rangle$, and $|\psi_v\rangle$ those for the valence electrons. Then

$$\hat{H}|\psi_n\rangle = E_n|\psi_n\rangle \ , \tag{6.42}$$

with $n = c, v$. The valence orbitals can be written as the sum of a smooth function (called the pseudo wave-function), $|\varphi_v\rangle$, with an oscillating function that results from the orthogonalization of the valence to the inner core orbitals

$$|\psi_v\rangle = |\varphi_v\rangle + \sum_c \alpha_{cv}|\psi_c\rangle \ , \tag{6.43}$$

where

$$\alpha_{cv} = -\langle\psi_c|\varphi_v\rangle \ . \tag{6.44}$$

The Schrödinger equation for the smooth orbital $|\varphi_v\rangle$ leads to

$$\hat{H}|\varphi_v\rangle = E_v|\varphi_v\rangle + \sum_c (E_c - E_v)|\psi_c\rangle\langle\psi_c|\varphi_v\rangle \ . \tag{6.45}$$

This equation indicates that states $|\varphi_v\rangle$ satisfy a Schrödinger-like equation with an energy-dependent pseudo-Hamiltonian

$$\hat{H}^{\mathrm{PK}}(E) = \hat{H} - \sum_c (E_c - E)|\psi_c\rangle\langle\psi_c| \ . \tag{6.46}$$

It is then possible to identify

$$\hat{w}^{\mathrm{PK}}(E) = \hat{v} - \sum_c (E_c - E)|\psi_c\rangle\langle\psi_c| \,, \tag{6.47}$$

where $\hat{v}$ is the true potential, as the effective potential in which valence electrons move. However, this pseudo-potential is non-local and depends on the eigen-energy of the electronic state one wishes to find.

At a certain distance from the ionic core $\hat{w}^{\mathrm{PK}}$ becomes $\hat{v}$ due to the decay of the core orbitals. In the region near the core, the orthogonalization of the valence orbitals to the strongly oscillating core orbitals forces valence electrons to have a high kinetic energy (The kinetic energy density is essentially a measure of the curvature of the wave-function.) The valence electrons feel an effective potential which is the result of the screening of the nuclear potential by the core electrons, the Pauli repulsion and xc effects between the valence and core electrons. The second term of (6.47) represents then a repulsive potential, making the pseudo-potential much weaker than the true potential in the vicinity of the core. All this implies that the pseudo wave-functions will be smooth and will not oscillate in the core region, as desired.

A consequence of the cancellation between the two terms of (6.47) is the surprisingly good description of the electronic structure of solids given by the nearly-free electron approximation. The fact that many metal and semiconductor band structures are a small distortion of the free electron gas band structure suggests that the valence electrons do indeed feel a weak potential. The Phillips and Kleinman potential explains the reason for this cancellation.

The original pseudo-potential from Hellmann (6.41) can be seen as an approximation to the Phillips and Kleinman form, as in the limit $r \to \infty$ the last term can be approximated as $A\mathrm{e}^{-r/R}$, where R is a parameter measuring the core orbitals decay length.

The Phillips and Kleinman potential was later generalized [33,34] to

$$\hat{w} = \hat{v} + \sum_c |\psi_c\rangle\langle\xi_c| \,, \tag{6.48}$$

where ξ_c is some set of functions.

The pseudo-potential can be cast into the form

$$w(\boldsymbol{r}, \boldsymbol{r}') = \sum_l \sum_{m=-l}^{l} Y_{lm}^*(\hat{r}) w_l(r, r') Y_{lm}(\hat{r}') \,, \tag{6.49}$$

where Y_{lm} are the spherical harmonics. This expression emphasizes the fact that w as a function of r and r' depends on the angular momentum. The most usual forms for $w_l(r, r')$ are the separable Kleinman and Bylander form [35]

$$w_l(r, r') = v_l(r) v_l(r') \,, \tag{6.50}$$

and the semi-local form

$$w_l(r, r') = w_l(r)\delta(r - r') \; . \tag{6.51}$$

6.3.2 Empirical Pseudo-potentials

Until the late 70's the method employed to construct a pseudo-potential was based on the Phillips and Kleinman cancellation idea. A model analytic potential was constructed and its parameters were fitted to experimental data. However, these models did not obey condition (6.43).

One of the most popular model potentials was introduced by Heine and Abarenkov in 1964 [36,37,38]. The Heine-Abarenkov potential is

$$w^{\mathrm{HA}}(\boldsymbol{r}) = \begin{cases} -z/r & , \text{if } r > R \\ -A_l \hat{P}_l & , \text{if } r \leq R \; , \end{cases} \tag{6.52}$$

with $\hat{P}_l$ an angular momentum projection operator. The parameters A_l were adjusted to the excitation energies of valence electrons and the parameter R is chosen, for example, to make A_0 and A_1 similar (leading to a local pseudo-potential for the simple metals).

A simplification of the Heine-Abarenkov potential was proposed in 1966 by Ashcroft [39,40]

$$w^{\mathrm{A}}(\boldsymbol{r}) = \begin{cases} -z/r & , \text{if } r > R \\ 0 & , \text{if } r \leq R \; . \end{cases} \tag{6.53}$$

In this model potential it is assumed that the cancellation inside the core is perfect, i.e., that the kinetic term cancels exactly the Coulomb potential for $r < R$. To adjust R, Ashcroft used data on the Fermi surface and on liquid phase transport properties.

The above mentioned and many other model potentials are discontinuous at the core radius. This discontinuity leads to long-range oscillations of their Fourier transforms, hindering their use in plane-wave calculations. A recently proposed model pseudo-potential overcomes this difficulty: the evanescent core potential of Fiolhais *et al.* [41]

$$w^{\mathrm{EC}}(r) = -\frac{z}{R}\left\{\frac{1}{x}\left[1 - (1 + \beta x)\exp^{-\alpha x}\right] - A\exp^{-x}\right\} \; , \tag{6.54}$$

with $x = r/R$, where R is a decay length and $\alpha > 0$. Smoothness of the potential and the rapid decay of its Fourier transform are guaranteed by imposing that the first and third derivatives are zero at $r = 0$, leaving only two parameters to be fitted (α and R). These are chosen by imposing one of several conditions [41,42,43,44,45,46]: total energy of the solid is minimized at the observed electron density; the average interstitial electron density matches the all-electron result; the bulk moduli match the experimental results; etc.

Although not always bringing great advances, several other model potentials were proposed [47,48,49]. Also, many different methods for adjusting the parameters were suggested [50]. The main application of these model potentials was to the theory of metallic cohesion [51,52,53,54,55].

6.3.3 *Ab-initio* Pseudo-potentials

A crucial step toward more realistic pseudo-potentials was given by Topp and Hopfield [49,56], who suggested that the pseudo-potential should be adjusted such that they describe the valence charge density accurately. Based on that idea, modern pseudo-potentials are obtained inverting the free atom Schrödinger equation for a given reference electronic configuration [57], and forcing the pseudo wave-functions to coincide with the true valence wave-functions beyond a certain distance r_l. The pseudo wave-functions are also forced to have the same norm as the true valence wave-functions.

These conditions can be written as

$$\begin{aligned} R_l^{\mathrm{PP}}(r) &= R_{nl}^{\mathrm{AE}}(r) \qquad\qquad , \text{ if } r > r_l \\ \int_0^{r_l} \mathrm{d}r \, \left|R_l^{\mathrm{PP}}(r)\right|^2 r^2 &= \int_0^{r_l} \mathrm{d}r \, \left|R_{nl}^{\mathrm{AE}}(r)\right|^2 r^2 \text{ , if } r < r_l \text{ ,} \end{aligned} \tag{6.55}$$

where $R_l(r)$ is the radial part of the wave-function with angular momentum l, and PP and AE denote, respectively, the pseudo wave-function and the true (all-electron) wave-function. The index n in the true wave-functions denotes the valence level. The distance beyond which the true and the pseudo wave-functions are equal, r_l, is also l-dependent.

Besides (6.55), there are still two other conditions imposed on the pseudo-potential: the pseudo wave-functions should not have nodal surfaces and the pseudo energy-eigenvalues should match the true valence eigenvalues, i.e.,

$$\varepsilon_l^{\mathrm{PP}} = \varepsilon_{nl}^{\mathrm{AE}} \, . \tag{6.56}$$

The potentials thus constructed are called norm-conserving pseudo-potentials, and are semi-local potentials that depend on the energies of the reference electronic levels, $\varepsilon_l^{\mathrm{AE}}$.

In summary, to obtain the pseudo-potential the procedure is: i) The free atom Kohn-Sham radial equations are solved taking into account all the electrons, in some given reference configuration

$$\left[-\frac{1}{2}\frac{\mathrm{d}^2}{\mathrm{d}r^2} + \frac{l(l+1)}{2r^2} + v_{\mathrm{KS}}^{\mathrm{AE}}\left[n^{\mathrm{AE}}\right](r)\right] r R_{nl}^{\mathrm{AE}}(r) = \varepsilon_{nl}^{\mathrm{AE}} r R_{nl}^{\mathrm{AE}}(r) \, , \tag{6.57}$$

where a spherical approximation to Hartree and exchange and correlation potentials is assumed and relativistic effects are not considered. The Kohn-Sham potential, $v_{\mathrm{KS}}^{\mathrm{AE}}$, is given by

$$v_{\mathrm{KS}}^{\mathrm{AE}}\left[n^{\mathrm{AE}}\right](r) = -\frac{Z}{r} + v_{\mathrm{Hartree}}\left[n^{\mathrm{AE}}\right](r) + v_{\mathrm{xc}}\left[n^{\mathrm{AE}}\right](r) \, . \tag{6.58}$$

ii) Using norm-conservation (6.55), the pseudo wave-functions are determined. Their shape in the region $r < r_l$ needs to be previously defined, and it is here that many modern potentials differ from one another. iii) Knowing the pseudo wave-function, the pseudo-potential results from the inversion of the radial Kohn-Sham equation for the pseudo wave-function and the valence electronic density

$$w_{l,\mathrm{scr}}(r) = \varepsilon_l^{\mathrm{PP}} - \frac{l(l+1)}{2r^2} + \frac{1}{2rR_l^{\mathrm{PP}}(r)} \frac{\mathrm{d}^2}{\mathrm{d}r^2} \left[rR_l^{\mathrm{PP}}(r) \right] \ . \tag{6.59}$$

The resulting pseudo-potential, $w_{l,\mathrm{scr}}$, still includes screening effects due to the valence electrons that have to be subtracted to yield

$$w_l(r) = w_{l,\mathrm{scr}}(r) - v_{\mathrm{Hartree}} \left[n^{\mathrm{PP}} \right](r) - v_{\mathrm{xc}} \left[n^{\mathrm{PP}} \right](r) \ . \tag{6.60}$$

The cutoff radii, r_l, are not adjustable pseudo-potential parameters. The choice of a given set of cutoff radii establishes only the region where the pseudo and true wave-functions coincide. Therefore, the cutoff radii can be considered as a measure of the quality of the pseudo-potential. Their smallest possible value is determined by the location of the outermost nodal surface of the true wave-functions. For cutoff radii close to this minimum, the pseudo-potential is very realistic, but also very strong. If very large cutoff radii are chosen, the pseudo-potentials will be smooth and almost angular momentum independent, but also very unrealistic. A smooth potential leads to a fast convergence of plane-wave basis calculations [58]. The choice of the ideal cutoff radii is then the result of a balance between basis-set size and pseudo-potential accuracy.

6.3.4 Hamann Potential

One of the most used parameterizations for the pseudo wave-functions is the one proposed in 1979 by Hamann, Schlüter, and Chiang [59] and later improved by Bachelet, Hamann and Schlüter [60] and Hamann [61].

The method proposed consists of using an intermediate pseudo-potential, $\bar{w}_l(r)$, given by

$$\begin{aligned} \bar{w}_l(r) + v_{\mathrm{Hartree}} \left[n^{\mathrm{PP}} \right](r) + v_{\mathrm{xc}} \left[n^{\mathrm{PP}} \right](r) = \\ = v_{\mathrm{KS}}^{\mathrm{AE}} \left[n^{\mathrm{AE}} \right](r) \left[1 - f\left(\frac{r}{r_l} \right) \right] + c_l f\left(\frac{r}{r_l} \right) \ , \end{aligned} \tag{6.61}$$

where $f(x) = \mathrm{e}^{-x^\lambda}$, and $\lambda = 4.0$ [59] or $\lambda = 3.5$ [60,61]. The Kohn-Sham equations are solved using this pseudo-potential, and the constants c_l are adjusted in order to obey (6.56). Notice that the form of the wave-functions implies that (6.55) is verified for some $\tilde{r}_l > r_l$. As the two effective potentials are identical for $r > \tilde{r}_l$, and given the fast decay of $f(x)$, the intermediate

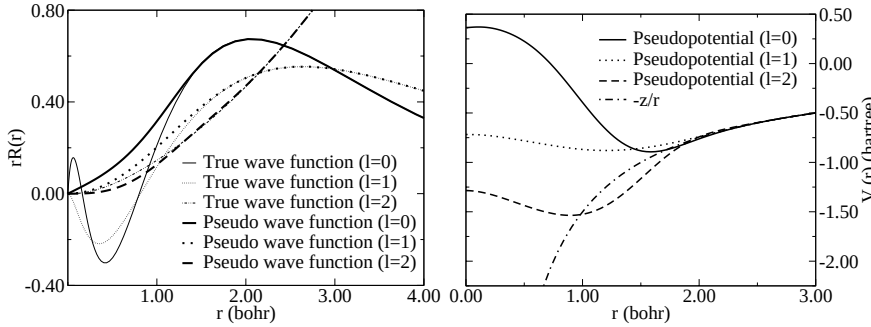

Fig. 6.2. Hamann pseudo-potential for Al, with $r_0 = 1.24$, $r_1 = 1.54$, and $r_2 = 1.40$ bohr: pseudo wave-functions vs. true wave-functions (left) and pseudo-potentials (right)

pseudo wave-functions, $\bar{R}_l(r)$, coincide, up to a constant, with the true wave-functions in that region.

In the method proposed by Hamann [61], the parameters c_l are adjusted so that

$$\frac{\mathrm{d}}{\mathrm{d}r} \ln \left[r R_{nl}^{\mathrm{AE}}(r) \right] \Big|_{r=\tilde{r}_l} = \frac{\mathrm{d}}{\mathrm{d}r} \ln \left[r \bar{R}_l(r) \right] \Big|_{r=\tilde{r}_l} . \tag{6.62}$$

This way, the method is not restricted to bound states.

To impose norm-conservation, the final pseudo wave-functions, $R_l^{\mathrm{PP}}(r)$, are defined as a correction to the intermediate wave-functions

$$R_l^{\mathrm{PP}}(r) = \gamma_l \left[\bar{R}_l(r) + \delta_l g_l(r) \right] , \tag{6.63}$$

where γ_l is the ratio $R_{nl}^{\mathrm{AE}}(r)/\bar{R}_l(r)$ in the region where $r > \tilde{r}_l$ and $g_l(r) = r^{l+1} f(r/r_l)$. The constants δ_l are adjusted to conserve the norm.

Figure 6.2 shows the Hamann pseudo-potential for Al, with $r_0 = 1.24$, $r_1 = 1.54$ and $r_2 = 1.40$ bohr. Note that the true and the pseudo wave-functions do not coincide at r_l – this only happens at $r > \tilde{r}_l$.

6.3.5 Troullier–Martins Potential

A different method to construct the pseudo wave-functions was proposed by Troullier and Martins [58,62], based on earlier work by Kerker [63]. This method is much simpler than Hamann's and emphasizes the desired smoothness of the pseudo-potential (although it introduces additional constraints to obtain it). It achieves softer pseudo-potentials for the $2p$ valence states of the first row elements and for the d valence states of the transition metals. For other elements both methods produce equivalent potentials.

The pseudo wave-functions are defined as

$$R_l^{\mathrm{PP}}(r) = \begin{cases} R_{nl}^{\mathrm{AE}}(r) & , \text{if } r > r_l \\ r^l \mathrm{e}^{p(r)} & , \text{if } r < r_l \end{cases} , \tag{6.64}$$

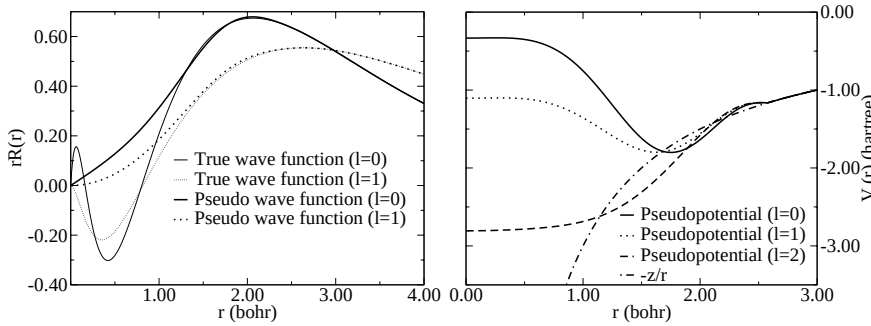

Fig. 6.3. Troullier-Martins pseudo-potential for Al, with $r_0 = r_1 = r_2 = 2.60\,\text{bohr}$: pseudo wave-functions vs. true wave-functions (left) and pseudo-potentials (right)

with

$$p(r) = c_0 + c_2 r^2 + c_4 r^4 + c_6 r^6 + c_8 r^8 + c_{10} r^{10} + c_{12} r^{12} \,. \tag{6.65}$$

The coefficients of $p(r)$ are adjusted by imposing norm-conservation, the continuity of the pseudo wave-functions and their first four derivatives at $r = r_l$, and that the screened pseudo-potential has zero curvature at the origin. This last condition implies that

$$c_2^2 + c_4(2l+5) = 0 \,, \tag{6.66}$$

and is the origin of the enhanced smoothness of the Troullier and Martins pseudo-potentials.

Figure 6.3 shows the Troullier and Martins pseudo-potential for Al, with $r_0 = r_1 = r_2 = 2.60\,\text{bohr}$. The $3d$ wave-functions are not shown since the state is unbound for this potential.

There are many other not so widely used norm-conserving pseudo-potentials [64,65,66,67,68]. Note that, in some cases, norm-conservation was abandoned in favor of increased pseudo-potential smoothness [69].

6.3.6 Non-local Core Corrections

It is tempting to assume that the Kohn-Sham potential depends linearly on the density, so that the unscreening of the pseudo-potential can be performed as in (6.60). Unfortunately, even though the Hartree contribution is indeed linearly dependent on the density, the xc term is not

$$\begin{aligned} v_{\text{xc}}\left[n^{\text{AE}}\right](r) &\equiv v_{\text{xc}}\left[n^{\text{core}} + n^{\text{PP}}\right](r) \\ &\neq v_{\text{xc}}\left[n^{\text{core}}\right](r) + v_{\text{xc}}\left[n^{\text{PP}}\right](r) \,. \end{aligned} \tag{6.67}$$

In some cases, like the alkali metals, the use of a nonlinear core-valence xc scheme may be necessary to obtain a transferable pseudo-potential. In these

cases, the unscreened potential is redefined as

$$w_l(r) = w_{l,\mathrm{scr}}(r) - v_{\mathrm{Hartree}}\left[n^{\mathrm{PP}}\right](r) - v_{\mathrm{xc}}\left[\tilde{n}^{\mathrm{core}} + n^{\mathrm{PP}}\right](r)\,, \tag{6.68}$$

and the core density is supplied together with the pseudo-potential. In a code that uses pseudo-potentials, one has simply to add the valence density to the given atomic core density to obtain the xc potential. To avoid spoiling the smoothness of the potential with a rugged core density, usually a partial core density [70,71], $\tilde{n}^{\mathrm{core}}$, is built and supplied instead of the true core density

$$\tilde{n}^{\mathrm{core}}(r) = \begin{cases} n^{\mathrm{core}}(r) & \text{for } r \geq r_{\mathrm{nlc}} \\ P(r) & \text{for } r < r_{\mathrm{nlc}} \end{cases}\,. \tag{6.69}$$

The polynomial $P(r)$ decays monotonically and has vanishing first and second derivatives at the origin. At r_{nlc} it joins smoothly the true core density (it is continuous up to the third derivative). The core cutoff radius, r_{nlc}, is typically chosen to be the point where the true atomic core density becomes smaller that the atomic valence density. It can be chosen to be larger than this value but if it is too large the description of the non-linearities may suffer. Note that, as the word partial suggests,

$$\int_0^{r_{\mathrm{nlc}}} \mathrm{d}r\, \tilde{n}^{\mathrm{core}}(r)\, r^2 < \int_0^{r_{\mathrm{nlc}}} \mathrm{d}r\, n^{\mathrm{core}}(r)\, r^2\,. \tag{6.70}$$

These corrections are more important for the alkali metals and other elements with few valence electrons and core orbitals extending into the tail of the valence density (e.g., Zn and Cd).

In some cases, the use of the generalized gradient approximation (GGA) for exchange and correlation leads to the appearance of very short-ranged oscillations in the pseudo-potentials (see Fig. 6.4). These oscillations are artifacts of the GGA that usually disappear when non-local core corrections are considered. Nevertheless, they do not pose a real threat for plane-wave calculations, since they are mostly filtered out by the energy cutoff.

6.3.7 Pseudo-potential Transferability

A useful pseudo-potential needs to be transferable, i.e., it needs to describe accurately the behavior of the valence electrons in several different chemical environments. The logarithmic derivative of the pseudo wave-function determines the scattering properties of the pseudo-potential. Norm-conservation forces these logarithmic derivatives to coincide with those of the true wave-functions for $r > r_l$. In order for the pseudo-potential to be transferable, this equality should hold at all relevant energies, and not only at the energy, ε_l, for which the pseudo-potential was adjusted. Norm-conservation assures that this is fulfilled for the nearby energies, as [49,72]

$$\frac{\mathrm{d}}{\mathrm{d}\varepsilon_l}\frac{\mathrm{d}}{\mathrm{d}r}\ln R_l(r)\bigg|_{r=R} = -\frac{2}{r^2 R_l^2(r)}\int_0^R \mathrm{d}r\, \left|R_l(r)\right|^2 r^2\,. \tag{6.71}$$

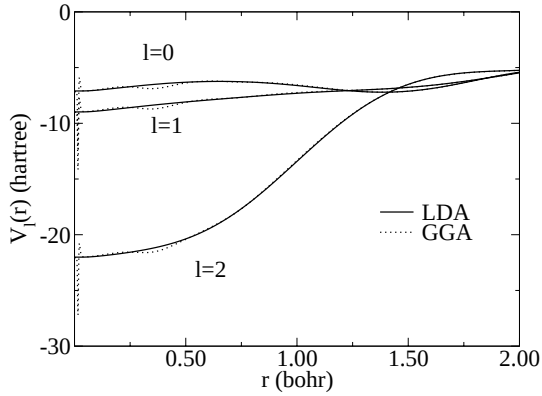

Fig. 6.4. Troullier-Martins pseudo-potential for Cu, with $r_0 = r_2 = 2.2$ and $r_1 = 2.4$ bohr. Notice that the LDA and GGA pseudo-potential are essentially identical, the main difference being the GGA potential oscillations near the origin

It is however necessary to take into account that the environment surrounding the electrons can be different from the one in the reference situation. Thus, although the pseudo-potential remains the same, the effective potential changes (the Hartree and xc potentials depend on the density). Therefore, the logarithmic derivative is not an absolute test of the transferability of a pseudo-potential [73]. The ideal method to assess the transferability of a potential consists in testing it in diverse chemical environments. The most usual way of doing this is to test its transferability to other atomic configurations and even to the ionized configurations. The variation of the total energy of the free atom with the occupancy of the valence orbitals is another test of transferability [74]. As the potential is generated for a given reference electronic configuration, it can be useful to choose the configuration that best resembles the system of interest [61]. However, the potential does not (should not) depend too much on the reference configuration.

6.3.8 Kleinman and Bylander Form of the Pseudo-potential

The semi-local form of the pseudo-potentials described above leads to a complicated evaluation of their action on a wave-function

$$\langle \boldsymbol{r} \,|\hat{w}|\, \Psi \rangle = \int \mathrm{d}^3 r' \, w(\boldsymbol{r}, \boldsymbol{r'}) \Psi(\boldsymbol{r'}) = \\ = \sum_l \sum_{m=-l}^{l} Y_{lm}(\hat{r}) w_l(r) \int \mathrm{d}^3 r' \, \delta(r - r') Y^*_{lm}(\hat{r}') \Psi(\boldsymbol{r'}) \; . \quad (6.72)$$

Unfortunately, the last integral must be calculated for each r. In a plane-wave expansion, this involves the product of an $N_{\mathrm{PW}} \times N_{\mathrm{PW}}$ matrix with the vector

representing the wave-function. This operation is of order $N_{\rm PW} \times N_{\rm PW}$, and $N_{\rm PW}$, the number of plane-waves in the basis set, can be very large.

The semi-local potential can be rewritten in a form that separates long and short range components. The long range component is local, and corresponds to the Coulomb tail. Choosing an arbitrary angular momentum component (usually the most repulsive one) and defining

$$\Delta w_l(r) = w_l(r) - w_{\rm local}(r) \; . \tag{6.73}$$

the pseudo-potential can be written as

$$w(\boldsymbol{r}, \boldsymbol{r}') = w_{\rm local}(r) + \sum_l \Delta w_l(r) \sum_{m=-l}^{l} Y_{lm}^*(\hat{r}') Y_{lm}(\hat{r}) \delta(r - r') \; . \tag{6.74}$$

Kleinman and Bylander [35] suggested that the non-local part of (6.74) are written as a separable potential, thus transforming the semi-local potential into a truly non-local pseudo-potential. If $\varphi_{lm}(\boldsymbol{r}) = R_l^{\rm PP}(r) Y_{lm}(\hat{r})$ denotes the pseudo wave-functions obtained with the semi-local pseudo-potential, the Kleinman and Bylander (KB) form is given by

$$\begin{aligned} w^{\rm KB}(\boldsymbol{r}, \boldsymbol{r}') &= w_{\rm local}(r) + \sum_l \Delta w_l^{\rm KB}(\boldsymbol{r}, \boldsymbol{r}') = \\ &= w_{\rm local}(r) + \sum_l \sum_{m=-l}^{l} \frac{\varphi_{lm}(\boldsymbol{r}) \Delta w_l(\boldsymbol{r}) \Delta w_l(\boldsymbol{r}') \varphi_{lm}(\boldsymbol{r}')}{\int {\rm d}^3 r \, \Delta w_l(\boldsymbol{r}) \left| \varphi_{lm}(\boldsymbol{r}) \right|^2} \; , \end{aligned} \tag{6.75}$$

which is, in fact, easier to apply than the semi-local expression.

The KB separable form has, however, some disadvantages, leading sometimes to solutions with nodal surfaces that are lower in energy than solutions with no nodes [75,76]. These (ghost) states are an artifact of the KB procedure. To eliminate them one can use a different component of the pseudo-potential as the local part of the KB form or choose a different set of core radii for the pseudo-potential generation. As a rule of thumb, the local component of the KB form should be the most repulsive pseudo-potential component. For example, for the Cu potential of Fig. 6.4, the choice of $l = 2$ as the local component leads to a ghost state, but choosing instead $l = 0$ remedies the problem.

6.4 Atomic Calculations

As our first example we will present several atomic calculations. These simple systems will allow us to gain a fist impression of the capabilities and limitations of DFT. To solve the Kohn-Sham equations we used the code of J. L. Martins [77]. The results are then compared to Hartree-Fock calculations performed with GAMESS [78]. As an approximation to the xc potential, we

Table 6.1. Ionization potentials calculated either by taking the difference of total energies between the neutral and the singly ionized atom (diff.), or from the eigenvalue of the highest occupied orbital (HOMO). We note that in the case of Hartree-Fock, $-\varepsilon_{\rm HOMO}$ is only an approximation to the ionization potential

	LDA		GGA		Hartree-Fock		
atom	diff.	$-\varepsilon_{\rm HOMO}$	diff.	$-\varepsilon_{\rm HOMO}$	diff.	$-\varepsilon_{\rm HOMO}$	expt.
H	0.479	0.269	0.500	0.279	0.500	0.500	0.500
Ar	0.586	0.382	0.581	0.378	0.543	0.590	0.579
Hg	0.325	0.205	0.311	0.194	0.306	0.320	0.384
Hg (rel)	0.405	0.261	0.391	0.249		0.320	0.384

took the LDA, in the parameterization of Perdew and Zunger [6], and one GGA, flavor Perdew, Becke and Ernzerhof [79]. Furthermore, all calculations were done within the spin-polarized version of DFT.

The simplest atom one can study is hydrogen. As hydrogen has only one electron, its ground-state can be obtained analytically. One could expect that DFT yields precise results for such a trivial case. Surprisingly this is not true for several of the functionals currently in use, such as the LDA or most of the GGAs. In Table 6.1 we present calculations of the ionization potential (IP) for hydrogen. We note that in Kohn-Sham theory there are at least two ways to determine this quantity: (i) The eigenvalue of the highest occupied Kohn-Sham state is equal to minus the ionization potential, IP $= -\varepsilon_{\rm HOMO}$; (ii) By using the definition of the IP as the difference of total energies, IP $= E({\rm X}^+) - E({\rm X})$, where X is the atomic species. Even though the IPs calculated from (ii) come out fairly well for both LDA and GGA (the GGA are, in fact, slightly better), the $-\varepsilon_{\rm HOMO}$ are far too small, almost by a factor of two. On the other hand, Hartree-Fock is exact for this one-electron problem. To explain this discrepancy we have to take a closer look at the xc potential. As hydrogen has only one electron, the Kohn-Sham potential has to reduce to the external potential, $-1/r$. This implies that the xc for hydrogen is simply $v_{\rm xc}(\boldsymbol{r}) = -v_{\rm Hartree}(\boldsymbol{r})$. More precisely, it is the exchange potential that cancels the Hartree potential, while the correlation is zero. In the LDA and the GGA, neither of these conditions is satisfied. It is, however, possible to solve the hydrogen problem exactly within DFT by using some more sophisticated xc potentials, like the exact exchange [80], or the self-interaction corrected LDA [6] functionals.

Our first many-electron example is argon. Argon is a noble gas with the closed shell configuration $1s^2 2s^2 2p^6 3s^2 3p^6$, so its ground-state is spherical. In Fig. 6.5 we plot the electron density for this atom as a function of the distance to the nucleus. The function $n(r)$ decays monotonically, with very little structure, and is therefore not a very elucidative quantity to behold. However, if we choose to represent $r^2 n(r)$, we can clearly identify the shell structure of the atom: Three maxima, corresponding to the center of the three shells,

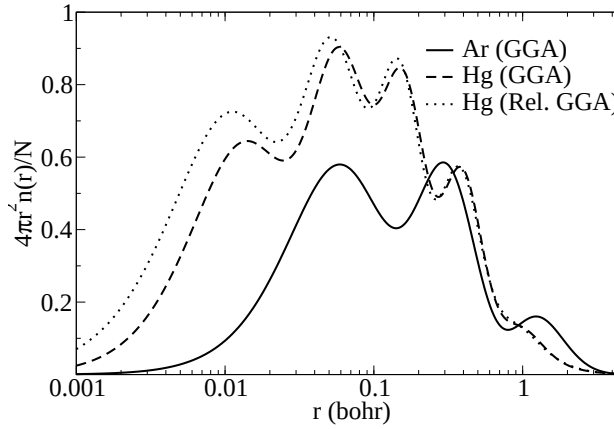

Fig. 6.5. Radial electronic density of the argon and mercury atoms versus the distance to the nucleus. Both the solid and dashed curves were obtained using the GGA to approximate the xc potential. For comparison the density resulting from a relativistic GGA calculation for mercury is also shown. The density is normalized so that the area under each curve is 1

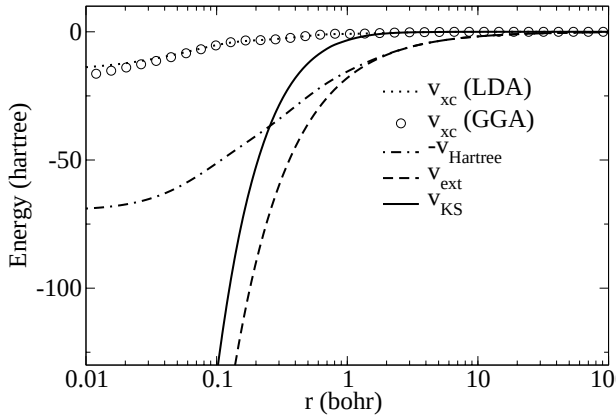

Fig. 6.6. LDA and GGA xc potentials for the argon atom. The dashed-dotted line corresponds to minus the Hartree potential evaluated with the GGA density. The LDA Hartree potential is however indistinguishable from this curve. Furthermore, the dashed line represents the argon nuclear potential, $-18/r$, and the solid line the total Kohn-Sham potential

and two minima separating these regions. The xc correlation potential used in the calculation was the GGA, but the LDA density looks almost indistinguishable from the GGA density. This is a fairly general statement – the LDA and most of the GGAs (as well as other more complicated functionals) yield very similar densities in most cases. The potentials and the energies can nevertheless be quite different.

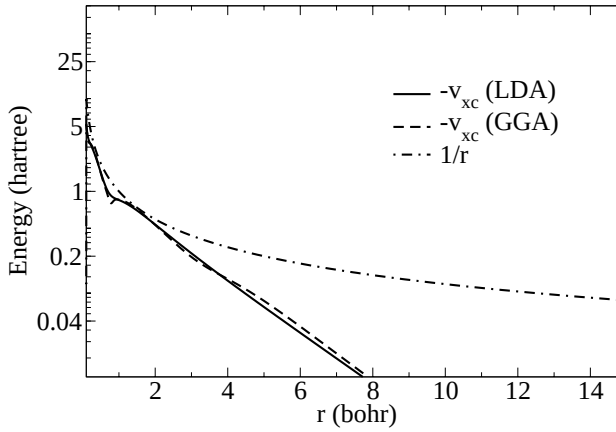

Fig. 6.7. LDA and GGA xc potentials for the argon atom in a logarithmic scale. For the sake of comparison we also plot the function $1/r$

Having the density it is a simple task to compute the Hartree and xc potentials. These, together with the nuclear potential $v_{\rm ext}(r) = -Z/r$, are depicted in Fig. 6.6. The Hartree potential is always positive and of the same order as the external potential. On the other hand, the xc potential is always negative and around 5 times smaller. Let us now suppose that an electron is far away from the nucleus. This electron feels a potential which is the sum of the nuclear potential and the potential generated by the remaining $N-1$ electrons. The further away from the nucleus, the smaller will be the dipole and higher-moment contributions to the electric field. It is evident from these considerations that the Kohn-Sham potential has to decay asymptotically as $-(Z-N+1)/r$. As the external potential decays as $-Z/r$, and the Hartree potential as N/r, one readily concludes that the xc potential has to behave asymptotically as $-1/r$. In fact it is the exchange part of the potential that has to account for this behavior, whilst the correlation potential decays with a higher power of $1/r$. To better investigate this feature, we have plotted, in logarithmic scale, $-v_{\rm xc}$, in the LDA and GGA approximations, together with the function $1/r$ (see Fig. 6.7). Clearly both the LDA and the GGA curve have a wrong (exponential) asymptotic behavior. From the definition of the LDA, (see 6.9), it is quite simple to derive this fact. The electronic density for a finite system decays exponentially for large distances from the nucleus. The quantity $\varepsilon^{\rm HEG}$ entering the definition is, as mentioned before, a simple function, not much more complicated than a polynomial. By simple inspection, it is then clear that inserting an exponentially decaying density in (6.9) yields an exponentially decaying xc potential.

The problem of the exponential decay can yet be seen from a different perspective. For a many-electron atom the Hartree energy can be written, in

terms of the Kohn-Sham orbitals, as

$$E_{\text{Hartree}} = \frac{1}{2}\int \mathrm{d}^3 r \int \mathrm{d}^3 r' \sum_{ij}^{\text{occ}} \frac{|\varphi_i(\boldsymbol{r})|^2 |\varphi_j(\boldsymbol{r}')|^2}{|\boldsymbol{r}-\boldsymbol{r}'|} \,. \tag{6.76}$$

Note that in the sum the term with $i = j$ is *not* excluded. This diagonal represents the interaction of one electron with itself, and is therefore called the self-interaction term. It is clearly a spurious term, and is exactly canceled by the diagonal part of the exchange energy. It is easy to see that neither the LDA nor the GGA exchange energy cancel exactly the self-interaction. This is, however, not the case in more sophisticated functionals like the exact exchange or the self-interaction-corrected LDA.

The self-interaction problem is responsible for some of the failures of the LDA and the GGA, namely (i) the too small ionization potentials when calculated from $\varepsilon_{\text{HOMO}}$; (ii) the non-existence of Rydberg series; (iii) the incapacity to bind extra electrons, thus rendering almost impossible the calculation of electron-affinities (EA).

In Table 6.1 we show the IPs calculated for the argon atom. It is again evident that $-\varepsilon_{\text{HOMO}}$ is too small [failure (i)], while the IPs obtained through total energy differences are indeed quite close to the experimental values, and in fact better than the Hartree-Fock results. Note that the LDA result is too large, but is corrected by the gradient corrections. This is again a fairly universal feature of the LDA and the GGA: The LDA tends to overestimate energy barriers, which are then corrected by the GGA to values closer to the experimental results.

Up to now we have disregarded relativistic corrections in our calculations. These, however, become important as the atomic number increases. To illustrate this fact, we show in Fig. 6.5 the radial electronic density of mercury ($Z = 80$) and in Table 6.1 its IP obtained from both a relativistic and a non-relativistic calculation. From the plot it is clear that the density changes considerably when introducing relativistic corrections, especially close to the nucleus, where these corrections are stronger. Furthermore, the relativistic IP is much closer to the experimental value. But, what do we mean by "relativistic corrections"? Even though a relativistic version of DFT (and relativistic functionals) have been proposed (see the chapter by R. Dreizler in this volume), very few calculations were performed within this formalism. In the context of standard DFT, "relativistic" calculation normally means the solution of a: (a) Dirac-like equation but adding a non-relativistic xc potential; (b) Pauli equation, i.e., including the mass polarization, Darwin and spin-orbit coupling terms; (c) Scalar-relativistic Pauli equation, i.e., including the mass polarization, Darwin and either ignoring the spin-orbit term, or averaging it; (d) ZORA equation (see [81,82]). Our calculations were performed with the recipe (a).

To complete this section on atomic calculations, we would like to take a step back and look at the difficulty in calculating electronic affinities (EA)

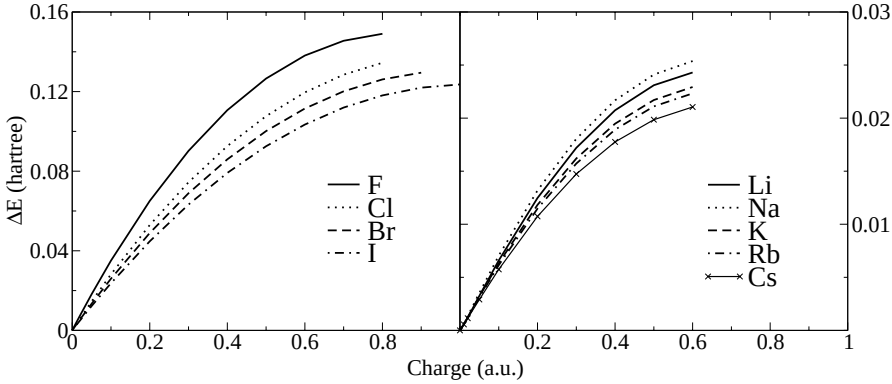

Fig. 6.8. $E(X) - E(X^{-\alpha})$ versus α for the halogen and alkali atoms

within the LDA and the GGA. For that purpose we performed GGA calculations for several atomic species, namely the halogen and alkali series, that we charged with a fraction, α, of an extra electron. The results are summarized in Fig. 6.8, where we depicted the difference of total energies between the charged and the neutral species, $E(X) - E(X^{-\alpha})$. Only Iodine was able to accept a full extra electron, while all other atoms bounded between 0.5 and 0.7 electrons. Even though a "proper" calculation of the EA is not possible in these cases, practical recipes do exist. We can, e.g., extrapolate $E(X) - E(X^{-\alpha})$ to $\alpha = 1$, and use this value as an estimation of the EA. In Table 6.2 we show the EAs obtained through a very simple polynomial extrapolation. The results compare fairly well for the halogens, while for the alkali atoms they exhibit errors of around 30%. However, we would like to stress that the situation is far from satisfactory from the theoretical point of view, and can only be solved by using better xc functionals.

Table 6.2. Electronic affinities for the halogen and alkali atoms. All values were obtained from extrapolation of $E(X) - E(X^{-\alpha})$ to $\alpha = 1$, except in the case of iodine (the only of this set of atoms able to bind an extra electron)

	F	Cl	Br	I	Li	Na	K	Rb	Cs
DFT	0.131	0.139	0.131	0.123	0.0250	0.0262	0.0240	0.0234	0.0222
expt.	0.125	0.133	0.124	0.112	0.0227	0.0201	0.0184	0.0179	0.0173

6.5 Plane-Wave Calculations

In this section we will present some simple calculations using a plane-wave expansion of the Kohn-Sham orbitals [4]. The plane-wave basis set is or-

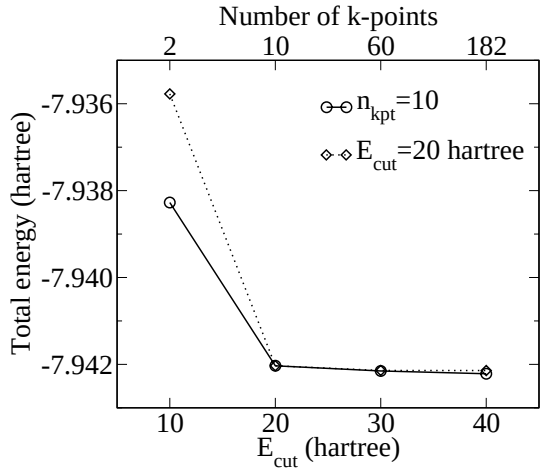

Fig. 6.9. Convergence of total energy of bulk Si with plane-wave energy cutoff and number of $\boldsymbol{k}$-points used in the sampling of the irreducible wedge of the Brillouin zone (within the LDA). The analysis of convergence with energy cutoff was done at a fixed Monkhorst-Pack sampling [23] using 10 $\boldsymbol{k}$-points, and the convergence with $\boldsymbol{k}$-point sampling was studied at a fixed energy cutoff of 20 hartree

thonormal and the convergence of the calculations increases systematically with the number of plane-waves. Gaussian basis sets, on the contrary, do not provide a clear and systematic way to improve the convergence of the calculations and do not form an orthonormal set. As a result, the calculations often depend on the choice of basis set. Another advantage of plane-waves is that the evaluation of forces for molecular dynamics is straightforward (the Pulay forces [83,11] are identically zero). These advantages lead the combination of pseudo-potentials, plane-waves, and Kohn-Sham equations to be known as the "standard model of solid-state theory".

As the first example of the use of a plane-wave expansion of the Kohn-Sham equations we shall calculate some properties of bulk silicon and examine its band-structure. All the results for bulk Si (diamond lattice) were obtained with a Troullier-Martins pseudo-potential with $r_0 = r_1 = r_2 = 1.89$ bohr. The local component used in the Kleinman and Bylander form of the pseudo-potential was the d-component. The variation of the total energy with respect to energy cutoff was assessed and a cutoff of 20 hartree was shown to lead to energies converged up to 0.001 hartree (see Fig. 6.9). The irreducible wedge of the Brillouin zone was sampled with different Monkhorst-Pack schemes [23] and the scheme using 10 $\boldsymbol{k}$-points was deemed sufficient to converge the total energy again up to 0.001 hartree.

The calculations for bulk silicon were done using both the LDA (Perdew-Wang 92 parameterization [7]) and the GGA (Perdew-Burke-Ernzerhof functional [79]). We note that we always used a pseudo-potential compatible with

Table 6.3. Comparison of some bulk properties of silicon obtained with the LDA and the GGA: equilibrium lattice constant (a), bulk modulus (B) and cohesive energy (E_c). Bulk moduli were obtained by fitting the Murnaghan equation of state [84] to the calculated total energy vs. volume curve. The experimental results (expt.) are those cited in [85]

	LDA	GGA	expt.
a (Å)	5.378	5.463	5.429
B (Mbar)	0.965	0.882	0.978
E_c (eV/atom)	6.00	5.42	4.63

the approximation for the xc potential,i.e., for the LDA calculations we used a pseudo-potential generated with the LDA, and the same for the GGA. Although sometimes there is no discernible difference between the results obtained with pseudo-potentials generated with different xc functionals (but using the same cutoffs), one should always use the same functional for the calculation as the one used in the generation of the pseudo-potential [71].

In Table 6.3 we summarize the results obtained for some bulk properties of silicon. It is immediately apparent that the LDA under-estimates the equilibrium lattice parameter, while the GGA over-estimates it. This is a typical result: the LDA, in general, over-binds by 1–2% and the GGA produces larger bond lengths, correcting the LDA, but sometimes over-corrects it. In the present case the GGA leads to a lattice parameter 0.5% larger than the experimental value. A similar statement can be made for the cohesive energy ($E_c = E_{\rm bulk}/N_{\rm atom} - E_{\rm atom}$): the LDA predicts a cohesive energy larger than the experimental value, and the GGA corrects it.

The band-structure of silicon obtained in this calculation is shown in Fig. 6.10. It was calculated at the LDA equilibrium lattice constant, even in the GGA case. These band-structures exhibit the well-known "band-gap problem" of DFT: the predicted band-gap is too small roughly by a factor of two. This is true for the LDA and the GGA. In fact, the GGA does not show a great improvement, even when the band-structure is calculated at its predicted equilibrium lattice constant (Table 6.4). The failure of these two DFT schemes in predicting the band-gap of silicon is not a surprise. Even if the true xc potential was known, the difference between the conduction and valence bands in a KS calculation would differ from the true band-gap (E_g). The true band-gap may be defined as the ground-state energy difference between the N and $N \pm 1$ systems

$$E_g = E(N+1) + E(N-1) - 2E(N) \; . \tag{6.77}$$

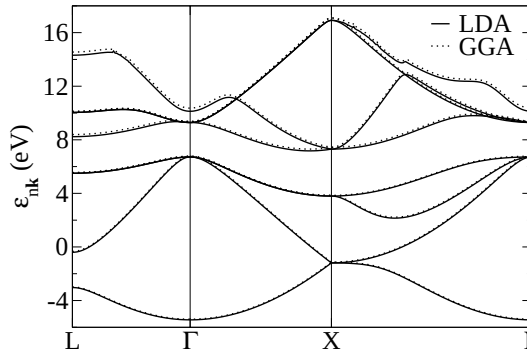

Fig. 6.10. Band structure of Si, obtained at the LDA equilibrium lattice constant

The difference between the highest occupied level and the lowest unoccupied level of the N-electron system is, on the other hand,

$$\begin{aligned} \varepsilon_{N+1}^{KS}(N) - \varepsilon_{N}^{KS}(N) &= E_g - \left[\varepsilon_{N+1}^{KS}(N+1) - \varepsilon_{N+1}^{KS}(N)\right] \\ &\equiv E_g - \Delta_{\mathrm{xc}} \ . \end{aligned} \tag{6.78}$$

Δ_{xc} is then a measure of the shift in the Kohn-Sham potential due to an infinitesimal variation of the density (in an extended system, the densities of the N and $N+1$ systems are almost identical). This shift is rigid (see the discussions in Chaps. 1 and 5), and is entirely due to a discontinuity in the derivative of the xc energy functional. It cannot therefore be accounted for by simple analytical, continuous approximations to exchange and correlation, like the LDA or the GGA. One could however argue that the error in the LDA band-gaps should come from two different sources: Δ_{xc} and the use of an approximate functional for exchange and correlation. If the latter were the most important, one could hope that better approximations would yield band-gaps in closer agreement with experiment. However, it appears that the "exact" Kohn-Sham band-gap does not differ much from the LDA band-gap, Δ_{xc} being the major culprit of the band-gap problem.

Usually, the LDA conduction bands are shifted from the correct bands by a quantity that is only weakly dependent on $\boldsymbol{k}$. A common solution to the band-gap problem is then to rigidly shift upward the Kohn-Sham conduction bands. This is called the "scissors operator".

A system which is much more difficult to handle within a first-principles pseudo-potential, plane-wave, density functional method is copper (as all the other noble and transition metals). Metals require a very good sampling of the irreducible wedge of the Brillouin zone in order to properly describe the Fermi surface. This makes them computationally more demanding. But copper presents yet another difficulty: It is mandatory that the $3d$-electrons are taken into account, as they contribute significantly to bonding and to the valence band structure. Therefore, these electrons cannot be frozen into the

Table 6.4. Comparison of the band-gap (E_g) and of gaps at some special points in the Brillouin zone (Γ, X and L). The column labeled GGA* refers to values obtained with the GGA at the LDA equilibrium lattice constant, and GGA labels the results obtained with the GGA at the GGA equilibrium lattice constant. The experimental results (expt.) are those cited in [86]. All values are in eV

	LDA	GGA*	GGA	expt.
E_g	0.45	0.53	0.61	1.17
Γ	2.57	2.59	2.57	3.34
X	3.51	3.59	3.56	1.25
L	2.73	2.84	2.64	2.4

Table 6.5. Lattice parameter (a), bulk modulus (B), and cohesive energy (E_c) of Cu, calculated with the LDA (Perdew-Wang 92 functional [7]) and GGA (Perdew-Burke-Ernzerhof functional [79]). Bulk moduli were obtained by fitting the Murnaghan equation of state [84] to the calculated total energy versus volume curve. The experimental results are those cited in [87]

	LDA	GGA	expt.
a (Å)	3.571	3.682	3.61
B (Mbar)	0.902	0.672	1.420
E_c (eV/atom)	4.54	3.58	3.50

core. However, their inclusion in the set of valence electrons means that there will be at least 11 valence electrons (one could also include the $3s$ and $3p$ electrons) and that the pseudo-potential will be very hard. The combination of these two factors makes the calculations almost prohibitive.

The use of soft pseudo-potentials like the Troullier-Martins pseudo-potential alleviates the problem. Table 6.5 and Fig. 6.11 show some results for bulk Cu obtained with a Troullier-Martins pseudo-potential with $r_0 = r_2 = 2.05\,\text{bohr}$ and $r_1 = 2.30\,\text{bohr}$. The local component used in the Kleinman and Bylander form of the pseudo-potential was the s-component and a partial core correction was included with $r_{\text{nlc}} = 0.8\,\text{bohr}$. The pseudo-potential thus obtained is soft enough to allow for well converged plane-wave calculations with an energy cutoff of 60 hartree. The Brillouin zone was sampled with a Monkhorst-Pack scheme using 60 $\boldsymbol{k}$-points and a Gaussian broadening of the levels with a 0.01 hartree width. The convergence of the calculations against energy cutoff, $\boldsymbol{k}$-point sampling and width of the smearing gaussian was better than 0.001 hartree. The calculations were done using both the LDA and the GGA for exchange and correlation. The LDA used was the Perdew-Wang 92 [7] parameterization of the Ceperley-Alder results [5] and the GGA was the Perdew-Burke-Ernzerhof [79] functional. As in the case of silicon, and for the sake of consistency, the pseudo-potentials employed in both calculations were consistent with the xc functional.

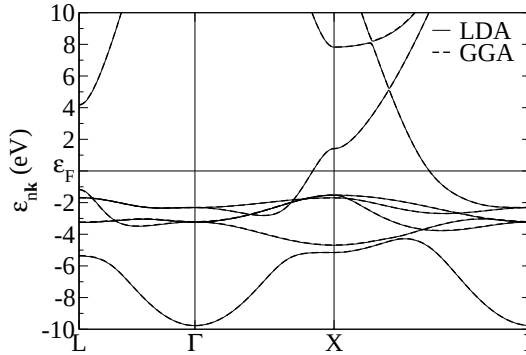

Fig. 6.11. Calculated band structure of Cu, obtained at the LDA equilibrium lattice constant

Table 6.6. Theoretical band-widths and energies at some high symmetry points in the Brillouin zone. The column labeled GGA* refers to values obtained with the GGA at the LDA equilibrium lattice constant, and GGA labels the results obtained with the GGA at the GGA equilibrium lattice constant. Results are compared to a GW calculation [88] and to averages over several experiments [89] (expt.). All values are in eV

		LDA	GGA*	GGA	GW	expt.
Positions of d bands	Γ_{12}	−2.31	−2.31	−2.12	−2.81	−2.78
	X_5	−1.53	−1.53	−1.44	−2.04	−2.01
	L_3	−1.68	−1.69	−1.58	−2.24	−2.25
Widths of d bands	$\Gamma_{12} - \Gamma_{25'}$	0.91	0.90	0.78	0.60	0.81
	$X_5 - X_3$	3.17	3.15	2.73	2.49	2.79
	$X_5 - X_1$	3.62	3.62	3.14	2.90	3.17
	$L_3 - L_3$	1.57	1.56	1.34	1.26	1.37
	$L_3 - L_1$	3.69	3.66	3.23	2.83	2.91
Positions of s, p bands	Γ_1	−9.77	−9.77	−9.02	−9.24	−8.60
	$L_{2'}$	−1.16	−1.19	−0.88	−0.57	−0.85
L gap	$L_1 - L_{2'}$	4.21	4.16	3.92	4.76	4.95

From Table 6.5 it is apparent that the LDA predicted, as usual, a lattice parameter smaller than the experimental one, while the GGA over-corrected this error. The over-binding of the LDA is also present in the cohesive energy, which is 30% larger than the experimental value. The GGA fared much better, producing an error of only 2%.

From Table 6.6 one can see that the LDA predicts d bands that are more delocalized than the experimental ones and are also 0.5 eV closer to the Fermi level. As the LDA is supposed to work well only for smoothly

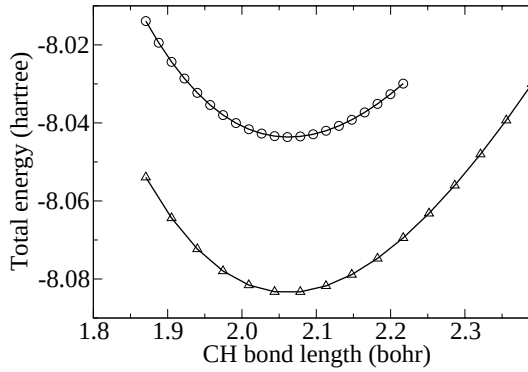

Fig. 6.12. Methane total energy vs. CH bond length: results obtained with the LDA (circles, Perdew-Wang 92 functional [7]) and the PBE [79] GGA (triangles). The Troullier-Martins pseudo-potential used for carbon had all the cutoff radii equal to 1.3 bohr. For hydrogen a pseudo-potential was also generated, with the same cutoff radii. Calculations were converged to better than 1 mhartree at an energy cutoff of 60 hartree and when using a 20 bohr cubic super-cell

varying densities, it comes at no surprise that highly localized states are not correctly described by it. The GGA does not improve on this result if the band-structure is calculated at the LDA lattice constant. If, however, one uses the predicted GGA lattice constant, then the width of the *d*-bands comes closer to the experimental values albeit getting even closer to the Fermi level. The GW results presented were calculated at the experimental lattice constant and show a very good agreement with experiment for the positions of the *d*-bands. Nevertheless, the widths of the bands are more precisely described by a much simpler GGA calculation.

As a last example of the use of plane-wave basis sets, we will look at methane. To deal with finite systems one has to resort to the super-cell technique. As we are using periodic boundary conditions, we will only be able to simulate a finite system if we place it inside a very large cell. If this cell is big enough, the system (molecule, cluster, etc.) will not interact with its periodic images. This means that, besides the usual convergence checks, one has also to check that the calculation converges with increasing cell size. Fortunately, in this case it is sufficient to use the Γ-point for sampling the irreducible wedge of the Brillouin zone.

The calculation of the equilibrium geometry is usually performed by minimizing the total energy using some conjugate-gradients (or more sophisticated) methods. However, for this simple example, we can just vary the CH bond length and plot the total energy. This is shown in Fig. 6.12.

From the energy curve it is also simple to extract the vibrational frequency of the CH bond. Close to the minimum, the energy depends quadratically on

Table 6.7. CH bond length and vibrational frequency (w) of the CH bond of CH_4, calculated with the LDA (Perdew-Wang 92 functional [7]) and GGA (Perdew-Burke-Ernzerhof functional [79])

	LDA	GGA	expt.
CH bond length (bohr)	2.06	2.06	2.04
w (cm^{-1})	3422	3435	2917

the bond length,

$$E \approx E_{\rm eq} + \frac{1}{2} m\omega^2 (r - r_{\rm eq})^2 \,, \tag{6.79}$$

where $E_{\rm eq}$ is the total energy at the equilibrium CH bond length ($r_{\rm eq}$), ω the vibrational frequency, and m is an "effective" mass of the system, which for this specific case reads

$$\frac{1}{m} = \frac{1}{m_{\rm C}} + \frac{1}{4m_{\rm H}} \,, \tag{6.80}$$

where $m_{\rm C}$ and $m_{\rm H}$ are the masses of the carbon and hydrogen atom, respectively. In Table 6.7 we summarize the results obtained for methane.

The results show that both the LDA and the GGA are over-estimating the CH bond length and the vibrational frequency. These calculations were repeated using a real-space method (see next section).

6.6 Real-Space Calculations

To illustrate the use of real-space methods, we again chose to study methane (CH_4). For all calculations, we used the program `octopus` [90] (see also `http://www.tddft.org/programs/octopus`), which was written by some of the authors, and is freely available under an open source license. Furthermore, we employed the Troullier-Martins pseudo-potentials which are distributed with the code, and the GGA in the parameterization of Perdew, Burke and Ernzerhof.

The first step of any calculation is the determination of the grid-spacing that is necessary to converge the energy to the required precision. This study is presented in Fig. 6.13. It is clear that the real-space technique is not variational, because the total energy does not decrease monotonically, but instead oscillates as we reduce the grid-spacing. To have the total energy and the Kohn-Sham eigenvalues converged to better than 0.005 hartree (≈ 0.1 eV) a grid-spacing of at least 0.35 bohr is necessary. This was therefore the grid-spacing we used to obtain the following results. Note that the optimum grid-spacing depends on the strength of the pseudo-potential used: The deeper the pseudo-potential, the tighter the mesh has to be.

The variation of the total energy with the C-H bond length is shown in Fig. 6.14. Remarkably, the calculated equilibrium C-H bond length, $r_{\rm eq}$,

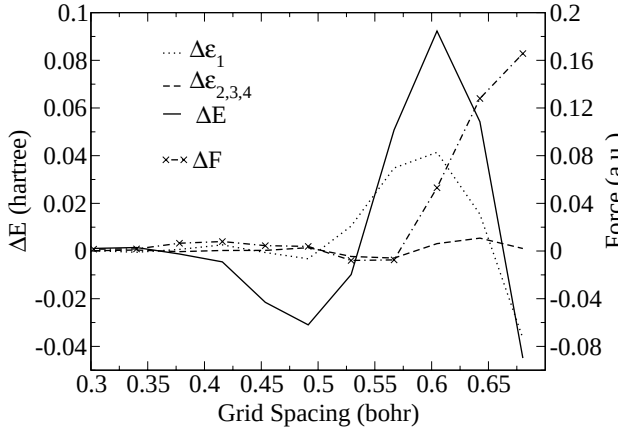

Fig. 6.13. Convergence of energies and forces versus grid-spacing. E is the total energy, F the absolute value of total force on a H atom, ε_1 the Kohn-Sham eigenvalue of the HOMO-1 state, and $\varepsilon_{2,3,4}$ the Kohn-Sham eigenvalue of the HOMO state (which is triply degenerate). For the sake of clarity, we plot the difference between these quantities and their converged values

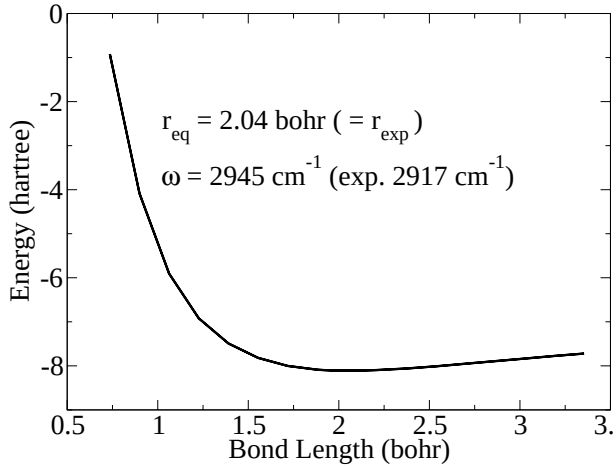

Fig. 6.14. Total energy of CH_4 versus C-H bond length

comes out on-top of the experimental value. The calculated value for the vibrational frequency of the CH bond ($\omega = 2945\,\mathrm{cm}^{-1}$) is slightly above the experimental result ($2917\,\mathrm{cm}^{-1}$), but the agreement is still very good.

For illustrative purposes we depict, in Fig. 6.15, the density and the Kohn-Sham orbitals of CH_4 in its equilibrium configuration. It is clear that very little information can be extracted by looking directly at the density, since it appears to be a very smooth function without any particular point of interest. It is therefore surprising that the density, by itself, is able to determine all

observables of the system. The Kohn-Sham eigenfunctions do not have any physical interpretation – they are simply mathematical objects used to obtain the electronic density. However, they do resemble very much to the traditional "molecular orbitals" used in chemistry, and are widely used as such. Note that the last three orbitals, (**c**), (**d**) and (**e**) are degenerate, and that the sum of their partial densities retains the tetrahedral symmetry of CH_4.

To conclude our section on real-space methods we present, in Fig. 6.16, a plot of the so-called "egg-box" effect. As mentioned before, the numerical grid breaks translational symmetry. This implies that the result of the calculation is dependent on where we position the molecule relatively to the grid. As most of the times the grids are uniform, the error will be periodic, with a period equal to the grid spacing. Plotting the error in the total energy as a function of the position of the molecule leads to a curve that resembles an egg-box. This error is inherent to all real-space implementations, but can be systematically reduced by decreasing the grid-spacing. In this particular case, the maximum "egg-box" error is of the order of 2 mhartree, for a grid spacing of 0.35 bohr. Clearly, the magnitude of the error increases for larger grid-spacings and stronger pseudo-potentials. Note that this "egg-box" effect leads to a spurious force term when performing molecular dynamics or geometry minimizations, so special care has to be taken in these cases.

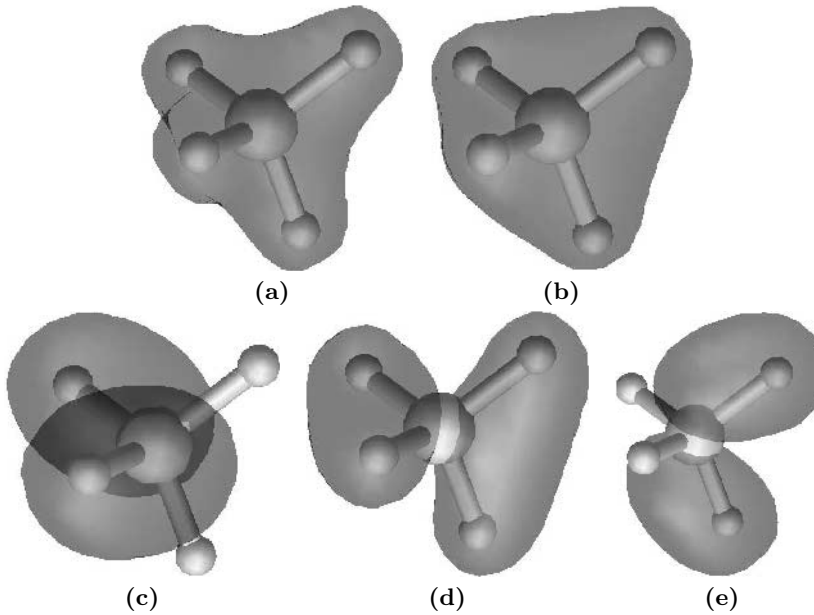

Fig. 6.15. Density **(a)**, HOMO-1 **(b)** and the 3 degenerate HOMO (**c**, **d** and **e**) Kohn-Sham orbitals of CH_4

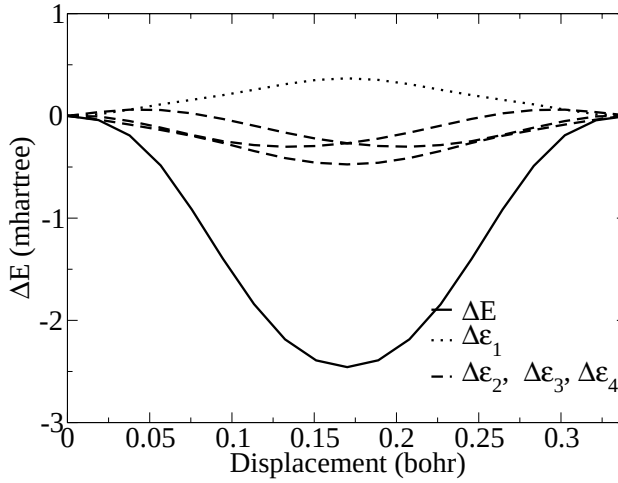

Fig. 6.16. Egg-box effect in CH_4. The x-axis represents the distance of the carbon atom to the central point of the grid. E is the total energy, ε_1 the Kohn-Sham eigenvalue of the HOMO-1 state, and $\varepsilon_{2,3,4}$ the Kohn-Sham eigenvalues of the HOMO state (which is triply degenerate). For the sake of clarity, we plot the difference between these quantities and their values when the carbon atom is located at the central grid-point

References

1. R. G. Parr and W. Yang, *Density-Functional Theory of Atoms and Molecules* (Oxford University Press, New York, 1989).
2. R. M. Dreizler and E. K. U. Gross, *Density Functional Theory: An Approach to the Quantum Many-Body Problem* (Springer-Verlag, Berlin, 1990).
3. The Free Software project for Atomic-scale Simulation aims at spreading the use of free software in atomic-scale simulations (URL `http://www.fsatom.org`).
4. The ABINIT code is a common project of the Université Catholique de Louvain, Corning Incorporated, the Université de Liège, the Commissariat à l'Energie Atomique, and other contributors (URL `http://www.abinit.org/`).
5. D. M. Ceperley and B. J. Alder, Phys. Rev. Lett. **45**, 566 (1980).
6. J. P. Perdew and A. Zunger, Phys. Rev. B **23**, 5048 (1981).
7. J. P. Perdew and Y. Wang, Phys. Rev. B **45**, 13244 (1992).
8. J. B. Krieger, Y. Li, and G. J. Iafrate, Phys. Rev. A **45**, 101 (1992).
9. D. G. Anderson, J. Assoc. Comput. Mach. **12**, 547 (1964).
10. D. R. Hamann, Phys. Rev. Lett. **42**, 662 (1979).
11. P. Pulay, Chem. Phys. Lett. **73**, 393 (1980).
12. C. G. Broyden, Math. Comp. **19**, 577 (1965).
13. D. D. Johnson, Phys. Rev. B **38**, 12807 (1988).
14. J. Ihm, A. Zunger, and M. L. Cohen, J. Phys. C: Solid State Phys. **12**, 4409 (1979), (E) *ibid.* **13** (1980) 3095.
15. J. Ihm, Rep. Prog. Phys. **51**, 105 (1988).
16. W. E. Pickett, Comp. Phys. Rep. **9**, 115 (1989).

17. N. Bingelli, J. L. Martins, and J. R. Chelikowsky, Phys. Rev. Lett. **68**, 2956 (1992).
18. M. R. Jarvis, I. D. White, R. W. Godby, and M. C. Payne, Phys. Rev. B **56**, 14972 (1997).
19. F. Nogueira, J. L. Martins, and C. Fiolhais, Eur. Phys. J. D **9**, 229 (2000).
20. A. Baldereschi, Phys. Rev. B **7**, 5212 (1973).
21. D. J. Chadi and M. L. Cohen, Phys. Rev. B **8**, 5747 (1973).
22. D. J. Chadi, Phys. Rev. B **16**, 1746 (1977).
23. H. J. Monkhorst and J. D. Pack, Phys. Rev. B **13**, 5188 (1976).
24. M. T. Yin and M. L. Cohen, Phys. Rev. B **26**, 3259 (1982).
25. T. L. Beck, Rev. Mod. Phys. **72**, 1041 (2000).
26. W. L. Briggs, *A Multigrid Tutorial* (SIAM, Philadelphia, 1987).
27. P. Wesseling, *An Introduction to Multigrid Methods* (Wiley, New York, 1992).
28. E. Fermi, Il Nuovo Cimento **11**, 157 (1934).
29. H. Hellmann, J. Chem. Phys. **3**, 61 (1935).
30. J. C. Phillips and L. Kleinman, Phys. Rev. **116**, 287 (1959).
31. L. Kleinman and J. C. Phillips, Phys. Rev. **118**, 1153 (1960).
32. E. Antončík, J. Phys. Chem. Solids **10**, 314 (1959).
33. M. H. Cohen and V. Heine, Phys. Rev. **122**, 1821 (1961).
34. B. J. Austin, V. Heine, and L. J. Sham, Phys. Rev. **127**, 276 (1962).
35. L. Kleinman and D. M. Bylander, Phys. Rev. Lett. **48**, 1425 (1982).
36. I. V. Abarenkov and V. Heine, Phil. Mag. **XII**, 529 (1965).
37. V. Heine and I. Abarenkov, Phil. Mag. **9**, 451 (1964).
38. A. O. E. Animalu and V. Heine, Phil. Mag. **12**, 1249 (1965).
39. N. W. Ashcroft, Phys. Lett. **23**, 48 (1966).
40. N. W. Ashcroft and D. C. Langreth, Phys. Rev. **155**, 682 (1967).
41. C. Fiolhais, J. P. Perdew, S. Q. Armster, J. M. MacLaren, and M. Brajczewska, Phys. Rev. B **51**, 14001 (1995), (E) *ibid.* **53** (1996) 13193.
42. F. Nogueira, C. Fiolhais, J. He, J. P. Perdew, and A. Rubio, J. Phys.: Condens. Matter **8**, 287 (1996).
43. C. Fiolhais, F. Nogueira, and C. Henriques, Prog. Surf. Sci. **53**, 315 (1996).
44. L. Pollack, J. P. Perdew, J. He, M. Marques, F. Nogueira, and C. Fiolhais, Phys. Rev. B **55**, 15544 (1997).
45. F. Nogueira, C. Fiolhais, and J. P. Perdew, Phys. Rev. B **59**, 2570 (1999).
46. J. P. Perdew, F. Nogueira, and C. Fiolhais, Theochem **9**, 229 (2000).
47. R. W. Shaw, Jr., Phys. Rev **174**, 769 (1968).
48. J. Callaway and P. S. Laghos, Phys. Rev. **187**, 192 (1969).
49. W. C. Topp and J. J. Hopfield, Phys. Rev. B **7**, 1295 (1973).
50. M. L. Cohen and V. Heine, Solid State Phys. **24**, 37 (1970).
51. W. A. Harrison, *Pseudopotentials in the Theory of Metals* (W. A. Benjamin, New York, 1966).
52. V. Heine and D. Weaire, Solid State Phys. **24**, 249 (1970).
53. J. Hafner and V. Heine, J. Phys. F.: Met. Phys. **13**, 2479 (1983).
54. J. Hafner and V. Heine, J. Phys. F: Met. Phys. **16**, 1429 (1986).
55. J. Hafner, *From Hamiltonians to Phase Diagrams* (Springer Verlag, Berlin, 1987).
56. T. Starkloff and J. D. Joannopoulos, Phys. Rev. B **16**, 5212 (1977).
57. A. Zunger and M. L. Cohen, Phys. Rev. B **18**, 5449 (1978).
58. N. Troullier and J. L. Martins, Phys. Rev. B **43**, 1993 (1991).

59. D. R. Hamann, M. Schlüter, and C. Chiang, Phys. Rev. Lett. **43**, 1494 (1979).
60. G. B. Bachelet, D. R. Hamann, and M. Schlüter, Phys. Rev. B **26**, 4199 (1982).
61. D. R. Hamann, Phys. Rev. B **40**, 2980 (1989).
62. N. Troullier and J. L. Martins, Solid State Commun. **74**, 613 (1990).
63. G. P. Kerker, J. Phys. C: Solid State Phys. **13**, L189 (1980).
64. E. L. Shirley, D. C. Allan, R. M. Martin, and J. D. Joannopoulos, Phys. Rev. B **40**, 3652 (1989).
65. A. M. Rappe, K. M. Rabe, E. Kaxiras, and J. D. Joannopoulos, Phys. Rev. B **41**, 1227 (1990).
66. G. Kresse, J. Hafner, and R. J. Needs, J. Phys.: Condens. Matter **4**, 7451 (1992).
67. A. M. Rappe and J. D. Joannopoulos, in *Computer Simulation in Materials Science*, edited by M. Meyer and V. Pontikis (Kluwer Academic Publishers, Dordrecht, 1991), pp. 409–422.
68. C. Hartwigsen, S. Goedecker, and J. Hutter, Phys. Rev. B **58**, 3641 (1998).
69. D. Vanderbilt, Phys. Rev. B **41**, 7892 (1990).
70. S. G. Louie, S. Froyen, and M. L. Cohen, Phys. Rev. B **26**, 1738 (1982).
71. M. Fuchs, M. Bockstedte, E. Pehlke, and M. Scheffler, Phys. Rev. B **57**, 2134 (1998).
72. R. W. Shaw, Jr. and W. A. Harrison, Phys. Rev. **163**, 604 (1967).
73. S. Goedecker and K. Maschke, Phys. Rev. A **45**, 88 (1992).
74. M. Teter, Phys. Rev. B **48**, 5031 (1993).
75. X. Gonze, P. Käckell, and M. Scheffler, Phys. Rev. B **41**, 12264 (1990).
76. X. Gonze, R. Stumpf, and M. Scheffler, Phys. Rev. B **44**, 8503 (1991).
77. URL `http://bohr.inesc.pt/~jlm/pseudo.html/`.
78. M. W. Schmidt, K. K. Baldridge, J. A. Boatz, S. T. Elbert, M. S. Gordon, J. J. Jensen, S. Koseki, N. Matsunaga, K. A. Nguyen, S. Su, T. L. Windus, M. Dupuis, and J. A. Montgomery, J. Comput. Chem. **14**, 1347 (1993).
79. J. P. Perdew, K. Burke, and M. Ernzerhof, Phys. Rev. Lett. **77**, 3865 (1996).
80. M. A. L. Marques, A. Castro, and A. Rubio, J. Chem. Phys. **115**, 3006 (2001).
81. C. Chang, M. Pélissier, and P. Durand, Phys. Scr. **34**, 394 (1986).
82. J. L. Heully, I. Lindgren, E. Lindroth, S. Lundqvist, and A. M. Mărtensson-Pendrill, J. Phys. B **19**, 2799 (1986).
83. P. Pulay, Mol. Phys. **17**, 197 (1969).
84. A. B. Alchagirov, J. P. Perdew, J. C. Boettger, R. C. Albers, and C. Fiolhais, Phys. Rev. B **63**, 224115 (2001).
85. T. J. Lenosky, J. D. Kress, I. Kwon, A. F. Voter, B. Edwards, D. F. Richards, S. Yang, and J. B. Adams, Phys. Rev. B **55**, 1528 (1997).
86. M. Städele, M. Moukara, J. A. Majewski, P. Vogl, and A. Görling, Phys. Rev. B **59**, 10031 (1999).
87. J. H. Rose, J. R. Smith, F. Guinea, and J. Ferrante, Phys. Rev. B **29**, 2963 (1984).
88. A. Marini, G. Onida, and R. D. Sole, Phys. Rev. Lett. **88**, 016403 (2002).
89. R. Courths and S. Hüfner, Phys. Rep. **112**, 53 (1984).
90. M. A. L. Marques, A. Castro, G. F. Bertsch, and A. Rubio, Comput. Phys. Commun. **151**, 60 (2003).